

# Cylindrical FDTD Analysis of LWD Tools Through Anisotropic Dipping Layered Earth Media

A Thesis

Presented in Partial Fulfillment of the Requirements for  
the Degree Master of Science in the  
Graduate School of The Ohio State University

By

Hwa Ok Lee, M.S.

\* \* \* \* \*

The Ohio State University

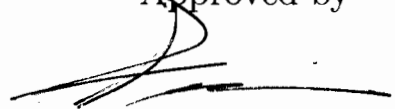
2005

Master's Examination Committee:

Fernando L. Texeira, Adviser

Prabhakar Pathak

Approved by



---

Adviser

Department of Electrical  
Engineering

© Copyright by

Hwa Ok Lee

2005

## ABSTRACT

Electrical Logging -While-Drilling(LWD) tools are an important part of oil and gas exploration to indicate the formation conductivity(resistivity) at different depths. The earth formation is exhibited as electric anisotropy with a fully  $3 \times 3$  tensor. Numerical methods have been developed to analyze the responses of the LWD tool in the 3-D anisotropic media. As a rule, a finite-difference time-domain(FDTD) method is flexible and efficient to model the geometry of the LWD tool in the geophysical formation. However, a basic finite-difference time-domain algorithm is limited to isotropic media. We discuss a 3-D cylindrical finite-difference time-domain algorithm with the fully anisotropy conductivity. The FDTD algorithm is validated by showing good agreement with the analytical results. We simulate the responses of the LWD tool in a 3-layer formation with an anisotropic dipping bed by using the 3-D anisotropic FDTD method.

Dedicated to my family and friends

## ACKNOWLEDGMENTS

I would like to thank my advisor, Prof. Fernando L. Teixeira for his endless patience. I could not accomplish my first goal at OSU without his guidance. Thanks to Prof. Prabhakar Pathak for his teaching and assistance. In addition, I thank my family and friends to encourage and trust me.

## VITA

April 7, 1975 ..... Born - Seoul, Korea.

February, 1998 ..... B.S. Electrical Engineering,  
DanKook University.

February, 2000 ..... M.S. Electrical Engineering,  
Microwave and Antenna Laboratory  
DanKook University.

2002-present ..... Electrical Engineering,  
The Ohio State University.

## FIELDS OF STUDY

Major Field: Electrical Engineering

# TABLE OF CONTENTS

	Page
Abstract . . . . .	ii
Dedication . . . . .	iii
Acknowledgments . . . . .	iv
Vita . . . . .	v
List of Figures . . . . .	viii
Chapters:	
1. Introduction . . . . .	1
1.1 Electrical Well Logging Tools . . . . .	2
1.2 Organization of This Thesis . . . . .	4
2. Anisotropic media . . . . .	5
2.1 Conductivity Tensor . . . . .	5
3. Nonuniform Cylindrical FDTD . . . . .	10
3.1 The FDTD Algorithm in Cylindrical Coordinates . . . . .	10
3.2 Periodic Boundary Condition in $\phi$ Coordinates . . . . .	18
3.3 Non-uniform grid in $\rho$ direction . . . . .	19
3.4 Numerical Stability . . . . .	20

4.	Extension . . . . .	22
4.1	Two Equations-Two Unknown Method . . . . .	22
4.2	Ramped Sine Excitations . . . . .	23
4.3	Cylindrical 3-D PML formulation . . . . .	24
5.	Numerical Simulations . . . . .	29
5.1	Logging-While-Drilling(LWD) Tool . . . . .	29
5.2	Apparent Resistivity . . . . .	31
5.3	Discretization . . . . .	33
5.4	Numerical Results . . . . .	34
5.4.1	Apparent Resistivity . . . . .	34
5.4.2	Borehole Effect . . . . .	37
5.4.3	Anisotropic Dipping Bed (True Vertical Thickness) . . . . .	43
5.4.4	Anisotropic Dipping Bed (Actual Thickness) . . . . .	53
6.	Summary and Conclusions . . . . .	60
Appendices:		
A.	Reference Result: LWD tool in infinitely thick bed with uniform conductivity	62
Bibliography . . . . .		65



## LIST OF FIGURES

Figure	Page
1.1 Basic configuration of LWD tool . . . . .	3
2.1 Relation between the logging tool reference and the anisotropy coordinates . . . . .	6
2.2 Azimuth relation between the logging tool and the anisotropy coordinates	7
3.1 Location of the electromagnetic field components on the cylindrical FDTD lattice . . . . .	12
3.2 The periodic boundary condition in $\phi$ direction . . . . .	18
3.3 Non-uniform discretization size along $\rho$ direction . . . . .	19
5.1 The basic structure of the LWD tool . . . . .	30
5.2 Apparent resistivities $R_{aph}$ and $R_{aam}$ for $\sigma_h = 0.1[\text{S/m}]$ without borehole versus anisotropy ratio. . . . .	35
5.3 Apparent resistivities $R_{aph}$ and $R_{aam}$ for $\sigma_h = 0.5[\text{S/m}]$ without borehole versus anisotropy ratio. . . . .	36
5.4 Phase Difference and Amplitude Ratio versus anisotropy ratio for $\sigma_h = 0.5[\text{S/m}]$ without Borehole. . . . .	38
5.5 Phase Difference and Amplitude Ratio versus anisotropy ratio for $\sigma_h = 0.5[\text{S/m}]$ with $\sigma_{mud} = 0.0005[\text{S/m}]$ . . . . .	39
5.6 Phase Difference and Amplitude Ratio versus anisotropy ratio for $\sigma_h = 0.5[\text{S/m}]$ with $\sigma_{mud} = 2[\text{S/m}]$ . . . . .	40

5.7	Phase Difference and Amplitude Ratio versus anisotropy ratio for $\sigma_h = 10[\text{S/m}]$ with $\sigma_{mud} = 0.0005[\text{S/m}]$ . . . . .	41
5.8	Phase Difference and Amplitude Ratio versus anisotropy ratio for $\sigma_h = 10[\text{S/m}]$ with $\sigma_{mud} = 2[\text{S/m}]$ . . . . .	42
5.9	Illustration of the LWD tool and a 3-layer formation with a true vertical thickness of dipping bed . . . . .	44
5.10	The effect of the horizontal conductivity in an inhomogeneous anisotropic dipping bed. . . . .	46
5.11	Simulation results of the LWD in an inhomogeneous isotropic dipping bed. . . . .	47
5.12	Simulation results of the LWD tool using $\sigma_{mud} = 2[\text{S/m}]$ crossing an inhomogeneous anisotropic dipping bed with $\sigma_h = 2.5$ , $\sigma_v = 0.5$ , and $\sigma_{iso} = 10[\text{S/m}]$ . (True vertical thickness) . . . . .	49
5.13	Simulation of the LWD using $\sigma_{mud} = 0.0005[\text{S/m}]$ crossing an inhomogeneous anisotropy dipping bed with $\sigma_h = 2.5$ , $\sigma_v = 0.5$ , and $\sigma_{iso} = 10[\text{S/m}]$ . (True vertical thickness) . . . . .	50
5.14	Simulation of the LWD tool using $\sigma_{mud} = 2[\text{S/m}]$ crossing an inhomogeneous anisotropic dipping bed with $\sigma_h = 10$ , $\sigma_v = 2.5$ , and $\sigma_{iso} = 0.5[\text{S/m}]$ . (True vertical thickness) . . . . .	51
5.15	Simulation of the LWD tool using $\sigma_{mud} = 0.0005[\text{S/m}]$ crossing an inhomogeneous anisotropic dipping bed with $\sigma_h = 10$ , $\sigma_v = 2.5$ , and $\sigma_{iso} = 0.5[\text{S/m}]$ . (True vertical thickness) . . . . .	52
5.16	Illustration of the LWD tool and a 3-layer formation with a actual thickness . . . . .	54
5.17	Simulation results of the LWD tool using $\sigma_{mud} = 2[\text{S/m}]$ crossing an inhomogeneous anisotropic dipping bed with $\sigma_h = 2.5$ , $\sigma_v = 0.5$ , and $\sigma_{iso} = 10[\text{S/m}]$ (Actual thickness). . . . .	56

5.18	Simulation results of the LWD tool using $\sigma_{mud} = 0.0005[\text{S/m}]$ in an inhomogeneous anisotropic dipping bed with $\sigma_h = 2.5$ , $\sigma_v = 0.5$ , and $\sigma_{iso} = 10[\text{S/m}]$ (Actual thickness). . . . .	57
5.19	Simulation results of the LWD tool using $\sigma_{mud} = 2[\text{S/m}]$ in an inhomogeneous anisotropic dipping bed with $\sigma_h = 10$ , $\sigma_v = 2.5$ , and $\sigma_{iso} = 0.5[\text{S/m}]$ (Actual thickness). . . . .	58
5.20	Simulation results of the LWD tool using $\sigma_{mud} = 0.0005[\text{S/m}]$ in an inhomogeneous anisotropic dipping bed with $\sigma_h = 10$ , $\sigma_v = 2.5$ , and $\sigma_{iso} = 0.5[\text{S/m}]$ (Actual thickness). . . . .	59
A.1	Illustration of a LWD tool in a homogeneous formation (infinitely thick bed) with an isotropic conductivity . . . . .	63
A.2	Simulation of the PD and AR of a LWD tool in an infinitely thick bed with different uniform conductivity, $\sigma_{mud} = 0.0005$ and $\sigma_{mud} = 2[\text{S/m}]$	64

# CHAPTER 1

## INTRODUCTION

Electromagnetic well-logging tools are used to investigate physical properties of complex earth formations in search of oil and gas reservoirs. EM logging tool response can be interpreted by collecting experiments in various situations. However, experiments are expensive and sometimes difficult to understand due to complicated effects dependent on various physical parameters. Alternatively, numerical methods have been developed to interpret the response of EM logging tool in complicated formations. Furthermore, numerical modeling can also be used to design EM logging tools.

Early modeling was very restricted by computer capabilities and limitations of analytical approaches. With advances in computer technologies, numerical methods become an important tool for the accurate interpretations of electromagnetic well-logging tool responses in 3-D inhomogeneous, anisotropic media.

Available numerical methods to predict responses of EM logging tools include, for example, BCGS-FFT [1], NMM [2], a time-domain transmission line matrix(TLM) [3] method, a finite-element method(FEM) [4], a finite-difference frequency-domain [5]-[6] and finite-difference time-domain(FDTD) [7]. In particular, the FEM and FDTD directly discretize Maxwell's equations. In the FEM, the solution region is discretized

into a number of finite elements conforming to the geometry of the problem. The individual finite elements are assembled into a set of large matrices. Then, the solution is obtained by solving the matrix equations. On the other hand, the FDTD using explicit time update equations has two main advantages. First, the implementation is easier than the FEM method and matrix inversion is not required. Second, FDTD in general requires less computer memory.

The property of interest in EM logging is an electric conductivity of the formation. In general, the conductivity is anisotropic and represented by a full  $3 \times 3$  tensor. However, the traditional FDTD method is restricted to an isotropy conductivity. If a fully anisotropy tensor is ignored, we can misunderstand the characteristics of geological structures due to the inadequate knowledge and interpretation errors in a complex formation.

## 1.1 Electrical Well Logging Tools

Electromagnetic logging tools are extensively used to measure the conductivity(resistivity) and the dielectric constant of a complex formation. A dielectric logging tool operating at a high frequency such as 1.1 GHz measures the travel time and attenuation and is able to extract the relative permittivity and the conductivity of the formation. However, such a tool provides investigation in limited depth because the conductivity attenuates the high frequency signal. On the other hand, a logging-while-drilling(LWD) tool operating at 2MHz primarily obtains conductivity(resistivity) of the formation. In the oil industry, an electric conductivity is the main parameter correlated to oil saturated media. Hence, we will be focusing on the LWD tool to compute electric conductivities. A typical LWD tool consists of one

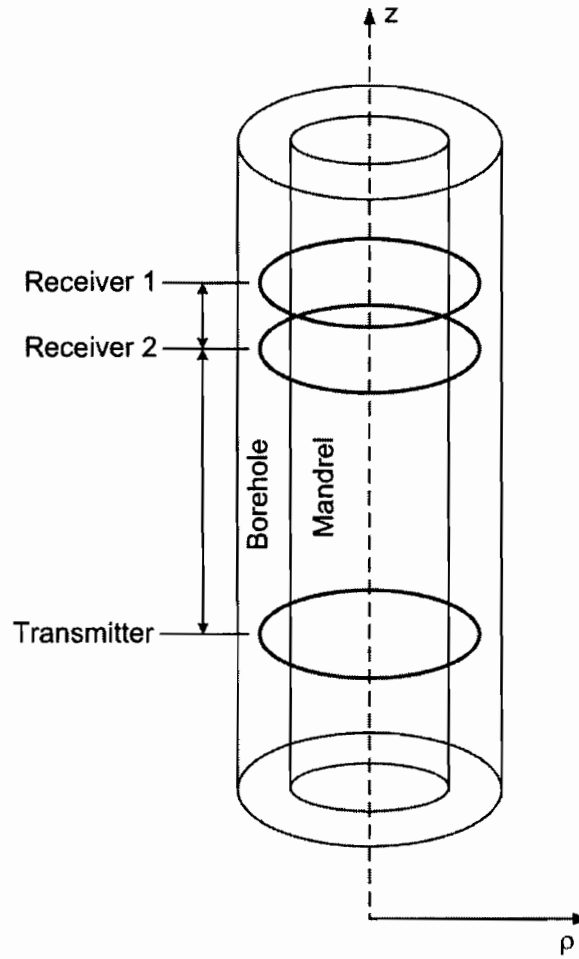


Figure 1.1: Basic configuration of LWD tool

transmitter and two receivers wound around a steel mandrel and inside a borehole as indicated in Figure 1.1. The transmitter wire antenna is operated at 2 MHz. Since the receiver voltages are affected by the physical properties of both the formation and the antenna characteristics, the antenna characteristics are usually compensated by taking the ratio of the two receiver voltages at each antenna. The voltage ratio is converted to an amplitude ratio and phase difference.

## 1.2 Organization of This Thesis

In this thesis, a 3-D FDTD method to simulate the responses of an EM well-logging tool in anisotropic formations is implemented. The FDTD method can be more efficient than other numerical methods to model a complex environment. The cylindrical coordinate system is chosen to reduce staircasing discretization errors due to the geometry of the EM logging tool. In the  $\rho$  direction, a nonuniform discretization is adopted to enlarge the size of the computation domain and increases the efficiency of the computer memory usage. A ramp sinusoidal function for a source at the transmitter is used in the FDTD algorithm to eliminate the DC offset and high frequency contamination. The data in the time domain at the two receivers are converted into a phase difference and amplitude ratio in the frequency domain by using two equations-two unknown method(2E2U) based on linear equations instead of traditional Fourier transform methods. We examine in Chapter2 the description of an anisotropy conductivity tensor with general oblique angles with respect to the tool coordinates. In Chapter3, a FDTD method is extended for a nonuniform cylindrical grid with a fully anisotropy tensor. Chapter4 discuss as the 2E2U method, an ramped sine excitation, and an anisotropic PML formulation in cylindrical coordinates used in the FDTD algorithm. In Chapter5, we present the simulated apparent resistivities from the responses of an EM logging tool in anisotropic media with infinitely thick bed and the simulated phase difference and amplitude ratio of an EM logging tool crossing a dipping bed with anisotropy conductivities for various dipping angles in a 3-layer formation. Chapter6 summarizes the conclusions and outlines the future work.

## CHAPTER 2

### ANISOTROPIC MEDIA

#### 2.1 Conductivity Tensor

Numerical simulations to analyze the response of electromagnetic well logging tools have been used to obtain accurate interpretations for various models of the earth formations. The important factor to incorporate in numerical simulations is the possible electric anisotropy of the earth formations with a conductivity tensor oriented along arbitrary directions. A generalized earth conductivity typically assumes that the electric conductivity tensor has nonzero elements only along the diagonal in the anisotropy axes. Thus, a  $3 \times 3$  anisotropy conductivity is simply expressed as

$$\bar{\sigma}' = \begin{bmatrix} \sigma_h & 0 & 0 \\ 0 & \sigma_h & 0 \\ 0 & 0 & \sigma_v \end{bmatrix} \quad (2.1)$$

where  $\sigma_h$  is the horizontal conductivity and  $\sigma_v$  is the vertical conductivity of the formation. These two conductivities can be different due to geological reasons, such as the gravitational pull. The anisotropy ratio is defined as

$$k = \left( \frac{\sigma_h}{\sigma_v} \right)^2 \quad (2.2)$$



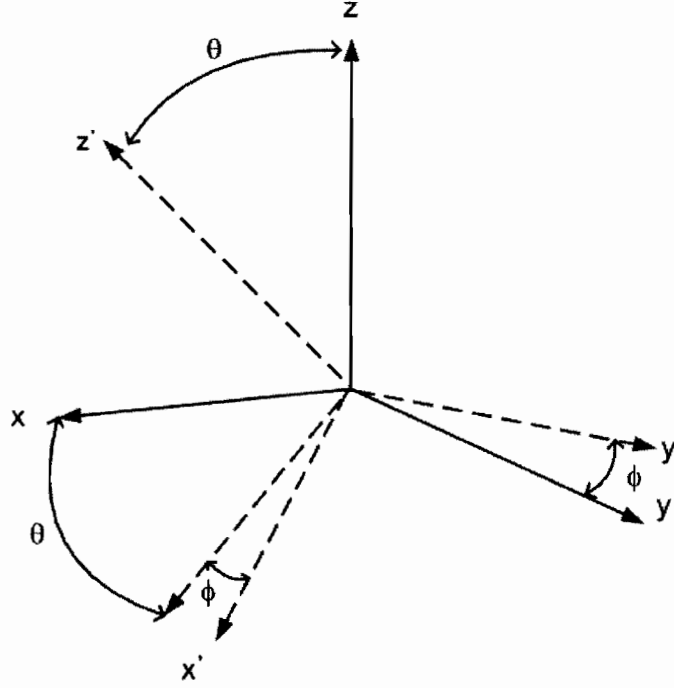


Figure 2.1: Relation between the logging tool reference and the anisotropy coordinates

When the anisotropy axes and the tool axes do not coincide, we can have a full  $3 \times 3$  tensor. The anisotropy axes are indicated by prime such as  $x'$ ,  $y'$ ,  $z'$  and the tool axes are the reference frame such as  $\rho$ ,  $\phi$ ,  $z$ . By using a rotation matrix, the conductivity tensor in the anisotropy coordinate system can be transferred to the tool coordinate system. The derivation of the rotation matrix is done with two rotations. First, an oblique angle  $\theta$  is defined by the rotation angle between  $z$  direction in the tool axes and  $z'$  direction in anisotropy axes as shown in Figure 2.1. The first rotation function by the oblique angle is easily obtained as

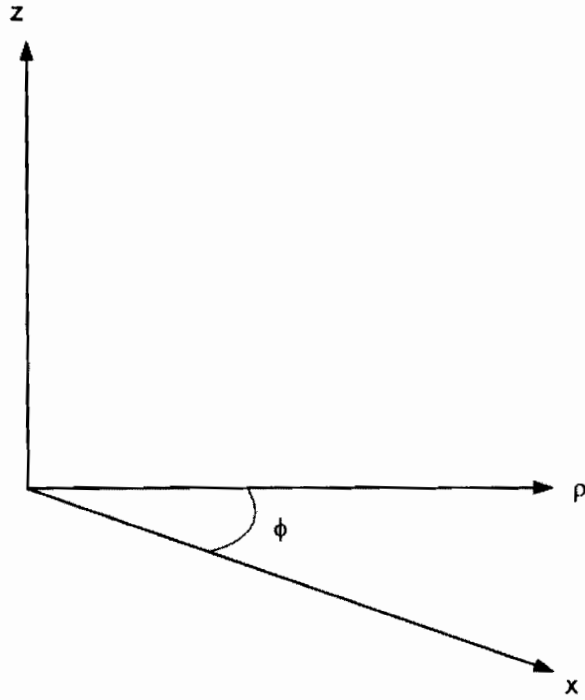


Figure 2.2: Azimuth relation between the logging tool and the anisotropy coordinates

$$R(\theta) = \begin{bmatrix} \cos \theta & 0 & -\sin \theta \\ 0 & 1 & 0 \\ \sin \theta & 0 & \cos \theta \end{bmatrix} \quad (2.3)$$

The second rotation referred to as transformation from the rectangular to cylindrical coordinate system is obtained by an azimuth angle  $\phi$  as shown in Figure 2.2. This is necessary because the cylindrical coordinate system is used since it conforms to geometry of the logging tool. Hence, a coordinate rotation as a function of positions in anisotropy media is expressed as

$$\begin{bmatrix} \rho' \\ \phi' \\ z' \end{bmatrix} = R(\theta, \phi) \begin{bmatrix} x \\ y \\ z \end{bmatrix} \quad (2.4)$$

where the rotation matrix  $R(\theta, \phi)$  is defined as

$$R(\theta, \phi) = \begin{bmatrix} \cos \theta \cos \phi & \cos \theta \sin \phi & -\sin \theta \\ -\sin \phi & \cos \phi & 0 \\ \sin \theta \cos \phi & \sin \theta \sin \phi & \cos \theta \end{bmatrix} \quad (2.5)$$

Now, the conductivity tensor  $\bar{\sigma}'$  in the anisotropy axes is transformed into  $\bar{\sigma}$  in the tool coordinates by the above rotation matrix  $R(\theta)$ . The constitutive relation in each coordinate system is given by

$$\begin{aligned} \mathbf{J} &= \bar{\sigma} \mathbf{E} \\ \mathbf{J}' &= \bar{\sigma}' \mathbf{E}' \end{aligned} \quad (2.6)$$

According to the rotation matrix  $R(\theta, \phi)$ , we have

$$\begin{aligned} R(\theta, \phi) \mathbf{J} &= \mathbf{J}' \\ R(\theta, \phi) \mathbf{E} &= \mathbf{E}' \end{aligned} \quad (2.7)$$

From (2.6) and (2.7), we have

$$R(\theta, \phi) \mathbf{J} = \mathbf{J}' = \bar{\sigma}' \mathbf{E}' = \bar{\sigma}' R(\theta, \phi) \mathbf{E}$$

$$\mathbf{J} = R^{-1}(\theta, \phi) \bar{\sigma}' R(\theta, \phi) \mathbf{E}$$

$$\bar{\sigma} \mathbf{E} = R^{-1}(\theta, \phi) \bar{\sigma}' R(\theta, \phi) \mathbf{E}$$

Thus, the conductivity tensor  $\bar{\sigma}$  in the logging tool coordinates becomes

$$\bar{\sigma} = R^{-1}(\theta, \phi) \bar{\sigma}' R(\theta, \phi) = \begin{bmatrix} \sigma_{\rho\rho} & \sigma_{\rho\phi} & \sigma_{\rho z} \\ \sigma_{\phi\rho} & \sigma_{\phi\phi} & \sigma_{\phi z} \\ \sigma_{z\rho} & \sigma_{z\phi} & \sigma_{zz} \end{bmatrix} \quad (2.8)$$

$$\begin{aligned} \sigma_{\rho\rho} &= \sigma_{\rho} \cos^2 \phi + \sigma_{\phi} \sin^2 \phi \\ \sigma_{\rho\phi} &= -\sigma_{\rho} \sin \phi \cos \phi + \sigma_{\phi} \sin \phi \cos \phi \\ \sigma_{\rho z} &= (\sigma_v - \sigma_h) \cos \phi \sin \theta \cos \theta \\ \sigma_{\phi\rho} &= -\sigma_{\rho} \cos \phi \sin \phi + \sigma_{\phi} \sin \phi \cos \phi \\ \sigma_{\phi\phi} &= \sigma_{\rho} \sin^2 \phi + \sigma_{\phi} \cos^2 \phi \\ \sigma_{\phi z} &= -(\sigma_v - \sigma_h) \sin \phi \sin \theta \cos \theta \\ \sigma_{z\rho} &= (\sigma_v - \sigma_h) \cos \phi \sin \theta \cos \theta \\ \sigma_{z\phi} &= -(\sigma_v - \sigma_h) \sin \phi \sin \theta \cos \theta \\ \sigma_{zz} &= \sigma_h \sin^2 \theta + \sigma_v \cos^2 \theta \end{aligned} \quad (2.9)$$

where

$$\begin{aligned} \sigma_{\rho} &= \sigma_h \cos^2 \theta + \sigma_v \sin^2 \theta \\ \sigma_{\phi} &= \sigma_h \end{aligned} \quad (2.10)$$

## CHAPTER 3

### NONUNIFORM CYLINDRICAL FDTD

#### 3.1 The FDTD Algorithm in Cylindrical Coordinates

The classic Yee scheme is usually applied to an isotropic medium in a Cartesian coordinate system [8]. Here, we consider a cylindrical coordinate system to conform the geometry of LWD tools. Furthermore, we incorporate anisotropic media with a  $3 \times 3$  conductivity tensor. Unfortunately, the basic Yee scheme does not automatically allow a fully anisotropy tensor in cylindrical coordinate system since it is restricted to diagonal elements. In this chapter, we discuss an extension of the FDTD algorithm for cylindrical coordinates and fully anisotropic medium. In an anisotropic medium the Maxwell's curl equations are given by

$$\nabla \times \mathbf{E} = -\mu \frac{\partial \mathbf{H}}{\partial t} - \mathbf{M} \quad (3.1)$$

$$\nabla \times \mathbf{H} = -\bar{\epsilon} \frac{\partial \mathbf{E}}{\partial t} + \bar{\sigma} \mathbf{E} + \mathbf{J} \quad (3.2)$$

where  $\mathbf{E}$  is the electric field in V/m,  $\mathbf{H}$  is the magnetic field in A/m,  $\mathbf{J}$  is the electric current density in A/m<sup>2</sup>,  $\mathbf{M}$  is the magnetic current density in V/m<sup>2</sup>,  $\mu$  is the permeability of the nonmagnetic medium. In cylindrical coordinates, a general anisotropic

medium has a  $3 \times 3$  permittivity and conductivity tensor,  $\bar{\epsilon}$  and  $\bar{\sigma}$  respectively, given by

$$\bar{\epsilon} = \begin{bmatrix} \epsilon_{\rho\rho} & \epsilon_{\rho\phi} & \epsilon_{\rho z} \\ \epsilon_{\phi\rho} & \epsilon_{\phi\phi} & \epsilon_{\phi z} \\ \epsilon_{z\rho} & \epsilon_{z\phi} & \epsilon_{zz} \end{bmatrix}, \quad \bar{\sigma} = \begin{bmatrix} \sigma_{\rho\rho} & \sigma_{\rho\phi} & \sigma_{\rho z} \\ \sigma_{\phi\rho} & \sigma_{\phi\phi} & \sigma_{\phi z} \\ \sigma_{z\rho} & \sigma_{z\phi} & \sigma_{zz} \end{bmatrix} \quad (3.3)$$

The six scalar equations of the vector equations (3.1) and (3.2) can be rewritten in the cylindrical coordinate system  $(\rho, \phi, z)$  as

$$\frac{1}{\rho} \frac{\partial E_z}{\partial \phi} - \frac{\partial E_\phi}{\partial z} = -\mu \frac{\partial H_\rho}{\partial t} - M_\rho \quad (3.4)$$

$$\frac{\partial E_\rho}{\partial z} - \frac{\partial E_z}{\partial \rho} = -\mu \frac{\partial H_\phi}{\partial t} - M_\phi \quad (3.5)$$

$$\frac{\partial E_\phi}{\partial \rho} + \frac{1}{\rho} E_\phi - \frac{1}{\rho} \frac{\partial E_\rho}{\partial \phi} = -\mu \frac{\partial H_z}{\partial t} - M_z \quad (3.6)$$

$$\frac{1}{\rho} \frac{\partial H_z}{\partial \phi} - \frac{\partial H_\phi}{\partial z} = \epsilon_{\rho\rho} \frac{\partial E_\rho}{\partial t} + \epsilon_{\rho\phi} \frac{\partial E_\phi}{\partial t} + \epsilon_{\rho z} \frac{\partial E_z}{\partial t} + \sigma_{\rho\rho} E_\rho + \sigma_{\rho\phi} E_\phi + \sigma_{\rho z} E_z + J_\rho \quad (3.7)$$

$$\frac{\partial H_\rho}{\partial z} - \frac{\partial H_z}{\partial \rho} = \epsilon_{\phi\rho} \frac{\partial E_\rho}{\partial t} + \epsilon_{\phi\phi} \frac{\partial E_\phi}{\partial t} + \epsilon_{\phi z} \frac{\partial E_z}{\partial t} + \sigma_{\phi\rho} E_\rho + \sigma_{\phi\phi} E_\phi + \sigma_{\phi z} E_z + J_\phi \quad (3.8)$$

$$\frac{\partial H_\phi}{\partial \rho} + \frac{1}{\rho} H_\phi - \frac{\partial H_\rho}{\partial \phi} = \epsilon_{z\rho} \frac{\partial E_\rho}{\partial t} + \epsilon_{z\phi} \frac{\partial E_\phi}{\partial t} + \epsilon_{zz} \frac{\partial E_z}{\partial t} + \sigma_{z\rho} E_\rho + \sigma_{z\phi} E_\phi + \sigma_{zz} E_z + J_z \quad (3.9)$$

In a cylindrical FDTD, a grid point is defined as

$$(i, j, k) = (i\Delta\rho, j\Delta\phi, k\Delta z) \quad (3.10)$$

and any function of the discretized space and time is represented as

$$F_{i,j,k}^n = F(i\Delta\rho, j\Delta\phi, k\Delta z, n\Delta t) \quad (3.11)$$

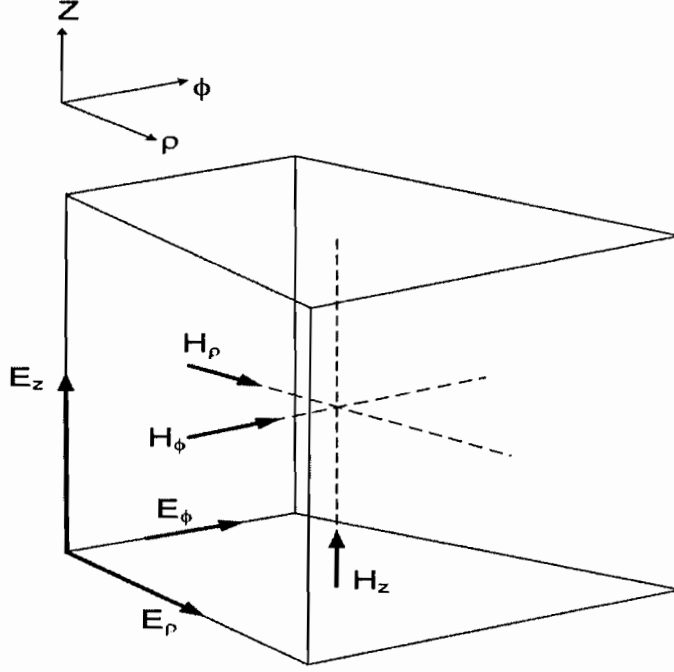


Figure 3.1: Location of the electromagnetic field components on the cylindrical FDTD lattice

where  $\Delta\rho$ ,  $j\Delta\phi$  and  $k\Delta z$  are the space increments,  $\Delta t$  is the time increment, and  $i, j, k$  and  $n$  are integers. Figure 3.1 illustrates the positions of the E and H discretizations using the three dimensional staggered FDTD grid scheme in cylindrical coordinates. Using central difference approximations for space and time derivatives, the spatial derivatives along  $\rho$  and time derivatives of any function  $F$  are

$$\frac{\partial F}{\partial \rho}(i\Delta\rho, j\Delta\phi, k\Delta z, n\Delta t) = \frac{F_{i+1/2,j,k}^n - F_{i-1/2,j,k}^n}{\Delta\rho} + O[(\Delta\rho)^2] \quad (3.12)$$

$$\frac{\partial F}{\partial t}(i\Delta\rho, j\Delta\phi, k\Delta z, n\Delta t) = \frac{F_{i,j,k}^{n+1/2} - F_{i,j,k}^{n-1/2}}{\Delta t} + O[(\Delta t)^2] \quad (3.13)$$

The locations of the  $E$  and  $H$  components are shown as Figure 3.1. Applying Eq.(3.12)-(3.13) into Eq.(3.4)-(3.9), the finite difference approximations for magnetic fields  $H_\rho$ ,  $H_\phi$ ,  $H_z$  at time  $n + 1/2$  and electric fields  $E_\rho$ ,  $E_\phi$ ,  $E_z$  on the time step  $n$  are obtained as

$$\begin{aligned} & \frac{1}{\Delta\rho_i} \left( \frac{E_{z(i,j+1,k+1/2)}^n - E_{z(i,j,k+1/2)}^n}{\Delta\phi} \right) - \left( \frac{E_{\phi(i,j+1/2,k+1)}^n - E_{\phi(i,j+1/2,k)}^n}{\Delta z_i} \right) \\ &= -\mu \left( \frac{H_{\rho(i,j+1/2,k+1/2)}^{n+1/2} - H_{\rho(i,j+1/2,k+1/2)}^{n-1/2}}{\Delta t} \right) - M_{\rho(i,j+1/2,k+1/2)}^n \end{aligned} \quad (3.14)$$

$$\begin{aligned} & \left( \frac{E_{\rho(i+1/2,j,k+1)}^n - E_{\rho(i+1/2,j,k)}^n}{\Delta z_i} \right) - \left( \frac{E_{z(i+1,j,k+1/2)}^n - E_{z(i,j,k+1/2)}^n}{\Delta\rho_i} \right) \\ &= -\mu \left( \frac{H_{\phi(i+1/2,j,k+1/2)}^{n+1/2} - H_{\phi(i+1/2,j,k+1/2)}^{n-1/2}}{\Delta t} \right) - M_{\phi(i+1/2,j,k+1/2)}^n \end{aligned} \quad (3.15)$$

$$\begin{aligned} & \left( \frac{E_{\phi(i+1,j+1/2,k)}^n - E_{\phi(i,j+1/2,k)}^n}{\Delta\rho_i} \right) + \frac{1}{\Delta\rho_{i+1/2}} \left[ E_{\phi(i+1/2,j+1/2,k)}^n \right. \\ & \left. - \left( \frac{E_{\rho(i+1/2,j+1,k)}^n - E_{\rho(i+1/2,j,k)}^n}{\Delta\phi} \right) \right] = -\mu \left( \frac{H_{z(i+1/2,j+1/2,k)}^{n+1/2} - H_{z(i+1/2,j+1/2,k)}^{n-1/2}}{\Delta t} \right) \\ & - M_{z(i+1/2,j+1/2,k)}^n \end{aligned} \quad (3.16)$$

$$\begin{aligned} & \frac{1}{\Delta\rho_{i+1/2}} \left( \frac{H_{z(i+1/2,j+1/2,k)}^{n+1/2} - H_{z(i+1/2,j-1/2,k)}^{n+1/2}}{\Delta\phi} \right) - \left( \frac{H_{\phi(i+1/2,j,k+1/2)}^{n+1/2} - H_{\phi(i+1/2,j,k-1/2)}^{n+1/2}}{\Delta z_i} \right) \\ &= \epsilon_{\rho\rho} \left( \frac{E_{\rho(i+1/2,j,k)}^{n+1} - E_{\rho(i+1/2,j,k)}^n}{\Delta t} \right) + \epsilon_{\rho\phi} \left( \frac{E_{\phi(i,j+1/2,k)}^{n+1} - E_{\phi(i,j+1/2,k)}^n}{\Delta t} \right) \\ &+ \epsilon_{\rho z} \left( \frac{E_{z(i,j,k+1/2)}^{n+1} - E_{z(i,j,k+1/2)}^n}{\Delta t} \right) + \sigma_{\rho\rho} E_{\rho(i+1/2,j,k)}^{n+1/2} + \sigma_{\rho\phi} E_{\phi(i,j+1/2,k)}^{n+1/2} + \sigma_{\rho z} E_{z(i,j,k+1/2)}^{n+1/2} \\ &+ J_{\rho(i+1/2,j,k)}^{n+1/2} \end{aligned} \quad (3.17)$$



$$\begin{aligned}
& \left( \frac{H_{\rho(i,j+1/2,k+1/2)}^{n+1/2} - H_{\rho(i,j+1/2,k-1/2)}^{n+1/2}}{\Delta z_i} \right) - \left( \frac{H_{z(i+1/2,j+1/2,k)}^{n+1/2} - H_{z(i-1/2,j+1/2,k)}^{n+1/2}}{\Delta \rho_i} \right) \\
&= \epsilon_{\phi\rho} \left( \frac{E_{\rho(i+1/2,j,k)}^{n+1} - E_{\rho(i+1/2,j,k)}^n}{\Delta t} \right) + \epsilon_{\phi\phi} \left( \frac{E_{\phi(i,j+1/2,k)}^{n+1} - E_{\phi(i,j+1/2,k)}^n}{\Delta t} \right) \\
&+ \epsilon_{\phi z} \left( \frac{E_{z(i,j,k+1/2)}^{n+1} - E_{z(i,j,k+1/2)}^n}{\Delta t} \right) + \sigma_{\phi\rho} E_{\rho(i+1/2,j,k)}^{n+1/2} + \sigma_{\phi\phi} E_{\phi(i,j+1/2,k)}^{n+1/2} + \sigma_{\phi z} E_{z(i,j,k+1/2)}^{n+1/2} \\
&+ J_{\phi(i,j+1/2,k)}^{n+1/2}
\end{aligned} \tag{3.18}$$

$$\begin{aligned}
& \left( \frac{H_{\phi(i+1/2,j,k+1/2)}^{n+1/2} - H_{\phi(i-1/2,j,k+1/2)}^{n+1/2}}{\Delta \rho_i} \right) \\
&+ \frac{1}{\Delta \rho_i} \left[ H_{\phi(i,j,k+1/2)}^{n+1/2} - \left( \frac{H_{\rho(i,j+1/2,k+1/2)}^{n+1/2} - H_{\rho(i,j-1/2,k+1/2)}^{n+1/2}}{\Delta \phi} \right) \right] \\
&= \epsilon_{z\rho} \left( \frac{E_{\rho(i+1/2,j,k)}^{n+1} - E_{\rho(i+1/2,j,k)}^n}{\Delta t} \right) + \epsilon_{z\phi} \left( \frac{E_{\phi(i,j+1/2,k)}^{n+1} - E_{\phi(i,j+1/2,k)}^n}{\Delta t} \right) \\
&+ \epsilon_{zz} \left( \frac{E_{z(i,j,k+1/2)}^{n+1} - E_{z(i,j,k+1/2)}^n}{\Delta t} \right) + \sigma_{z\rho} E_{\rho(i+1/2,j,k)}^{n+1/2} + \sigma_{z\phi} E_{\phi(i,j+1/2,k)}^{n+1/2} + \sigma_{zz} E_{z(i,j,k+1/2)}^{n+1/2} \\
&+ J_{z(i,j,k+1/2)}^{n+1/2}
\end{aligned} \tag{3.19}$$

The  $E$  components in the right sides of Eq.(3.17)-(3.19) at time step  $n + 1/2$  are replaced by semi-implicit approximations as follows

$$E_{\rho(i+1/2,j,k)}^{n+1/2} = \frac{E_{\rho(i+1/2,j,k)}^{n+1} + E_{\rho(i+1/2,j,k)}^n}{2} \tag{3.20}$$

$$E_{\phi(i,j+1/2,k)}^{n+1/2} = \frac{E_{\phi(i,j+1/2,k)}^{n+1} + E_{\phi(i,j+1/2,k)}^n}{2} \tag{3.21}$$

$$E_{z(i,j,k+1/2)}^{n+1/2} = \frac{E_{z(i,j,k+1/2)}^{n+1} + E_{z(i,j,k+1/2)}^n}{2} \tag{3.22}$$

Similarly, the undefined locations of  $E_{\phi(i+1/2,j+1/2,k)}^n$  and  $H_{\phi(i+1/2,j+1/2,k)}^{n+1/2}$  in Eq.(3.16) and (3.19) are substituted as follows

$$E_{\phi(i+1/2,j+1/2,k)}^n = \frac{E_{\phi(i+1,j+1/2,k)}^n + E_{\phi(i,j+1/2,k)}^n}{2} \quad (3.23)$$

$$H_{\phi(i,j,k+1/2)}^{n+1/2} = \frac{H_{\phi(i+1/2,j,k+1/2)}^{n+1/2} + H_{\phi(i-1/2,j,k+1/2)}^{n+1/2}}{2} \quad (3.24)$$

Using the above approximations, Eq.(3.17)-(3.19) are rearranged as

$$\begin{aligned} & \frac{1}{\Delta\rho_{i+1/2}} \left( \frac{H_{z(i+1/2,j+1/2,k)}^{n+1/2} - H_{z(i+1/2,j-1/2,k)}^{n+1/2}}{\Delta\phi} \right) - \left( \frac{H_{\phi(i+1/2,j,k+1/2)}^{n+1/2} - H_{\phi(i+1/2,j,k-1/2)}^{n+1/2}}{\Delta z_i} \right) \\ &= \left( \frac{\epsilon_{\rho\rho}}{\Delta t} + \frac{\sigma_{\rho\rho}}{2} \right) E_{\rho(i+1/2,j,k)}^{n+1} + \left( \frac{\epsilon_{\rho\phi}}{\Delta t} + \frac{\sigma_{\rho\phi}}{2} \right) E_{\phi(i,j+1/2,k)}^{n+1} + \left( \frac{\epsilon_{\rho z}}{\Delta t} + \frac{\sigma_{\rho z}}{2} \right) E_{z(i,j,k+1/2)}^{n+1} \\ &- \left( \frac{\epsilon_{\rho\rho}}{\Delta t} - \frac{\sigma_{\rho\rho}}{2} \right) E_{\rho(i+1/2,j,k)}^n - \left( \frac{\epsilon_{\rho\phi}}{\Delta t} - \frac{\sigma_{\rho\phi}}{2} \right) E_{\phi(i,j+1/2,k)}^n - \left( \frac{\epsilon_{\rho z}}{\Delta t} - \frac{\sigma_{\rho z}}{2} \right) E_{z(i,j,k+1/2)}^n \\ &+ J_{\rho(i+1/2,j,k)}^{n+1/2} \end{aligned} \quad (3.25)$$

$$\begin{aligned} & \left( \frac{H_{\rho(i,j+1/2,k+1/2)}^{n+1/2} - H_{\rho(i,j+1/2,k-1/2)}^{n+1/2}}{\Delta z_i} \right) - \left( \frac{H_{z(i+1/2,j,k+1/2)}^{n+1/2} - H_{z(i-1/2,j,k+1/2)}^{n+1/2}}{\Delta\rho_i} \right) \\ &= \left( \frac{\epsilon_{\phi\rho}}{\Delta t} + \frac{\sigma_{\phi\rho}}{2} \right) E_{\rho(i+1/2,j,k)}^{n+1} + \left( \frac{\epsilon_{\phi\phi}}{\Delta t} + \frac{\sigma_{\phi\phi}}{2} \right) E_{\phi(i,j+1/2,k)}^{n+1} + \left( \frac{\epsilon_{\phi z}}{\Delta t} + \frac{\sigma_{\phi z}}{2} \right) E_{z(i,j,k+1/2)}^{n+1} \\ &- \left( \frac{\epsilon_{\phi\rho}}{\Delta t} - \frac{\sigma_{\phi\rho}}{2} \right) E_{\rho(i+1/2,j,k)}^n - \left( \frac{\epsilon_{\phi\phi}}{\Delta t} - \frac{\sigma_{\phi\phi}}{2} \right) E_{\phi(i,j+1/2,k)}^n - \left( \frac{\epsilon_{\phi z}}{\Delta t} - \frac{\sigma_{\phi z}}{2} \right) E_{z(i,j,k+1/2)}^n \\ &+ J_{\phi(i,j+1/2,k)}^{n+1/2} \end{aligned} \quad (3.26)$$

$$\begin{aligned}
& \left( \frac{H_{\phi(i+1/2,j,k+1/2)}^{n+1/2} - H_{\phi(i-1/2,j,k+1/2)}^{n+1/2}}{\Delta \rho_i} \right) \\
& + \frac{1}{\Delta \rho_i} \left[ \left( \frac{H_{\phi(i+1/2,j,k+1/2)}^{n+1/2} + H_{\phi(i-1/2,j,k+1/2)}^{n+1/2}}{2} \right) - \left( \frac{H_{\rho(i,j+1/2,k+1/2)}^{n+1/2} - H_{\rho(i,j-1/2,k+1/2)}^{n+1/2}}{\Delta \phi} \right) \right] \\
& = \left( \frac{\epsilon_{z\rho}}{\Delta t} + \frac{\sigma_{z\rho}}{2} \right) E_{\rho(i+1/2,j,k)}^{n+1} + \left( \frac{\epsilon_{z\phi}}{\Delta t} + \frac{\sigma_{z\phi}}{2} \right) E_{\phi(i,j+1/2,k)}^{n+1} + \left( \frac{\epsilon_{zz}}{\Delta t} + \frac{\sigma_{zz}}{2} \right) E_{z(i,j,k+1/2)}^{n+1} \\
& - \left( \frac{\epsilon_{z\rho}}{\Delta t} - \frac{\sigma_{z\rho}}{2} \right) E_{\rho(i+1/2,j,k)}^n - \left( \frac{\epsilon_{z\phi}}{\Delta t} - \frac{\sigma_{z\phi}}{2} \right) E_{\phi(i,j+1/2,k)}^n - \left( \frac{\epsilon_{zz}}{\Delta t} - \frac{\sigma_{zz}}{2} \right) E_{z(i,j,k+1/2)}^n \\
& + J_{z(i,j,k+1/2)}^{n+1/2}
\end{aligned} \tag{3.27}$$

Note that the update equations for magnetic fields are in the well-known standard form because the nonmagnetic medium is assumed. However, the update equations to obtain the electric fields are expressed in matrix form. The final FDTD update equations can be written as

$$\begin{aligned}
H_{\rho(i,j+1/2,k+1/2)}^n &= H_{\rho(i,j+1/2,k+1/2)}^{n-1/2} + \frac{\Delta t}{\mu} \left[ \left( \frac{E_{\phi(i,j+1/2,k+1)}^n - E_{\phi(i,j+1/2,k)}^n}{\Delta z_i} \right) \right. \\
& \quad \left. - \frac{1}{\Delta \rho_i} \left( \frac{E_{z(i,j+1,k+1/2)}^n - E_{z(i,j,k+1/2)}^n}{\Delta \phi} \right) \right] - M_{\rho(i,j+1/2,k+1/2)}^n
\end{aligned} \tag{3.28}$$

$$\begin{aligned}
H_{\phi(i+1/2,j,k+1/2)}^{n+1/2} &= H_{\phi(i+1/2,j,k+1/2)}^{n-1/2} + \frac{\Delta t}{\mu} \left[ \left( \frac{E_{z(i+1,j,k+1/2)}^n - E_{z(i,j,k+1/2)}^n}{\Delta \rho_i} \right) \right. \\
& \quad \left. - \left( \frac{E_{\rho(i+1/2,j,k+1)}^n - E_{\rho(i+1/2,j,k)}^n}{\Delta z_i} \right) \right] - M_{\phi(i+1/2,j,k+1/2)}^n
\end{aligned} \tag{3.29}$$

$$\begin{aligned}
H_{z(i+1/2,j+1/2,k)}^{n+1/2} &= H_{z(i+1/2,j+1/2,k)}^{n-1/2} + \frac{\Delta t}{\mu} \left[ \frac{1}{\Delta \rho_{i+1/2}} \left( \frac{E_{\rho(i+1/2,j+1,k)}^n - E_{\rho(i+1/2,j,k)}^n}{\Delta \phi} \right) \right. \\
& \quad \left. - \left( \frac{E_{\phi(i+1,j+1/2,k)}^n + E_{\phi(i,j+1/2,k)}^n}{2} \right) - \left( \frac{E_{\phi(i+1,j+1/2,k)}^n - E_{\phi(i,j+1/2,k)}^n}{\Delta \rho_i} \right) \right] \\
& \quad - M_{z(i+1/2,j+1/2,k)}^n
\end{aligned} \tag{3.30}$$

$$\begin{bmatrix} E_{\rho(i+1/2,j,k)}^{n+1} \\ E_{\phi(i,j+1/2,k)}^{n+1} \\ E_{z(i,j,k+1/2)}^{n+1} \end{bmatrix} = \left( \frac{1}{\Delta t} \bar{\epsilon} + \frac{1}{2} \bar{\sigma} \right)^{-1}$$

$$\left\{ \begin{aligned} & \left[ \begin{aligned} & \frac{1}{\Delta \rho_{i+1/2}} \left( \frac{H_{z(i+1/2,j+1/2,k)}^{n+1/2} - H_{z(i+1/2,j-1/2,k)}^{n+1/2}}{\Delta \phi} \right) \\ & - \left( \frac{H_{\phi(i+1/2,j,k+1/2)}^{n+1/2} - H_{\phi(i+1/2,j,k-1/2)}^{n+1/2}}{\Delta z_i} \right) \\ & \left( \frac{H_{\rho(i,j+1/2,k+1/2)}^{n+1/2} - H_{\rho(i,j+1/2,k-1/2)}^{n+1/2}}{\Delta z_i} \right) \\ & - \left( \frac{H_{z(i+1/2,j,k+1/2)}^{n+1/2} - H_{z(i-1/2,j,k+1/2)}^{n+1/2}}{\Delta \rho_i} \right) \\ & \left( \frac{H_{\phi(i+1/2,j,k+1/2)}^{n+1/2} - H_{\phi(i-1/2,j,k+1/2)}^{n+1/2}}{\Delta \rho_i} \right) \\ & + \frac{1}{\Delta \rho_i} \left[ \left( \frac{H_{\phi(i+1/2,j,k+1/2)}^{n+1/2} + H_{\phi(i-1/2,j,k+1/2)}^{n+1/2}}{2} \right) \right. \\ & \left. - \left( \frac{H_{\rho(i,j+1/2,k+1/2)}^{n+1/2} - H_{\rho(i,j-1/2,k+1/2)}^{n+1/2}}{\Delta \phi} \right) \right] \end{aligned} \right] \\ & + \left( \frac{1}{\Delta t} \bar{\epsilon} - \frac{1}{2} \bar{\sigma} \right) \begin{bmatrix} E_{\rho(i+1/2,j,k)}^n \\ E_{\phi(i,j+1/2,k)}^n \\ E_{z(i,j,k+1/2)}^n \end{bmatrix} \end{aligned} \right\} \quad (3.31)$$

According to the finite difference expressions of Eq.(3.28)-(3.31), all electromagnetic field components at any location are obtained from the results of the past time step. Note that the 3-D cylindrical FDTD domain is discretized with  $(N_\rho, N_\phi, N_z)$  grid points. The discretizations of the  $\phi$  and  $z$  directions are uniform, but the  $\rho$  direction is discretized nonuniformly as discussed next.

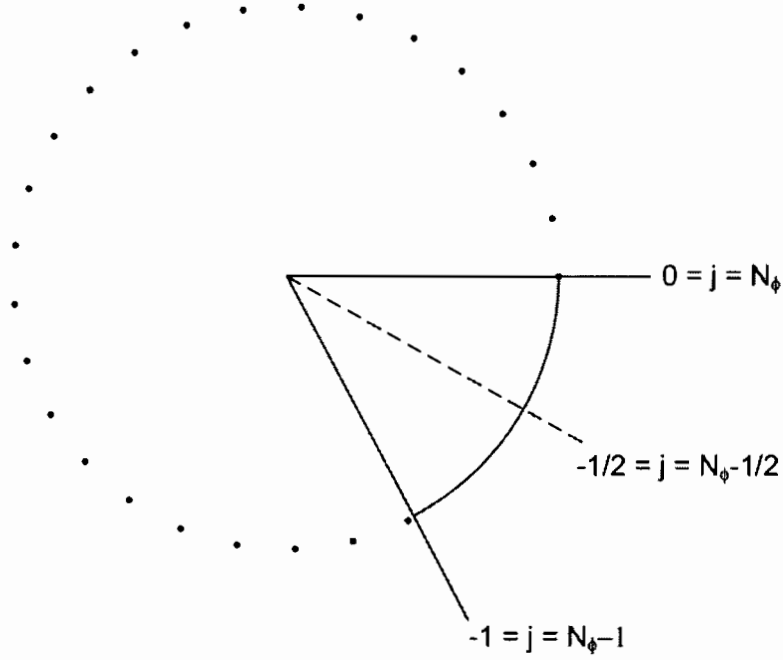


Figure 3.2: The periodic boundary condition in  $\phi$  direction

### 3.2 Periodic Boundary Condition in $\phi$ Coordinates

The  $\phi$  direction is discretized uniformly with a periodic boundary condition. As shown in Figure 3.2, the electric field components are identified at  $j = 0$  and  $j = N_\phi$ , and magnetic fields are identified at  $j = -1/2$  and  $j = N_\phi - 1/2$ . The appropriate grid size is important to reduce unnecessary time steps and to decide the largest cylindrical cell size. The outer cylindrical cell length along the  $\phi$  direction is given as

$$\Delta l_i = i \Delta \rho \Delta \phi \quad (3.32)$$

for  $i = N_\rho$ . However, the largest  $\Delta l$  should be chosen by the criteria below

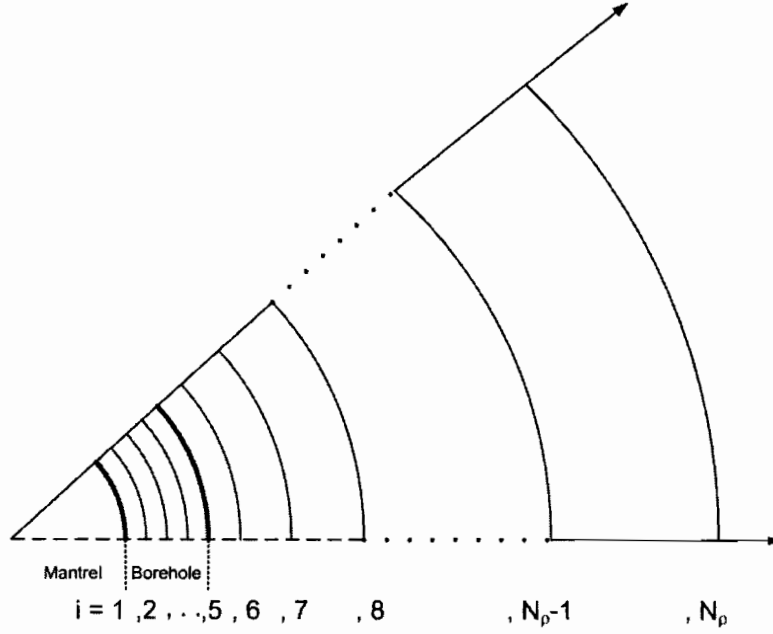


Figure 3.3: Non-uniform discretization size along  $\rho$  direction

$$\Delta l \leq \min \left( \frac{\delta}{6}, \frac{\lambda}{10} \right) \quad (3.33)$$

where  $\delta$  is the skin depth and  $\lambda$  is the wavelength in the formation. This set up a condition for choosing the maximum  $\Delta\phi$ ,  $\Delta\rho$  and  $\Delta z$ .

### 3.3 Non-uniform grid in $\rho$ direction

In the  $\rho$  direction, a nonuniform discretizations [9] is applied by increasing the  $\Delta\rho$  grid size gradually as shown in Figure 3.3. The computation domain along the  $\rho$  direction is divided into two regions. The region between the steel mandrel and the borehole wall is so small that a uniform discretization size is applied. In the other side, the discretization size increases nonuniformly because the formation outside a

logging tool is much larger. If uniform discretizations are used there, the required computer memories and computation time would be excessive. In diffusion dominated problems, the maximum grid size is defined as

$$(\Delta\rho)_{max} = \frac{\delta}{6} \quad (3.34)$$

where the skin depth  $\delta$  is given as

$$\delta = \frac{1}{\omega\sqrt{\mu\epsilon} \left\{ \frac{1}{2} \left[ \sqrt{1 + \left( \frac{\sigma}{\omega\epsilon} \right)^2} - 1 \right] \right\}^{1/2}} \quad (3.35)$$

where  $\omega$  is the angular frequency and the largest conductivity  $\sigma$  in the formation is chosen. For  $\frac{\sigma}{\omega\epsilon} \gg 1$ , Eq.(3.35) is simplified to

$$\delta = \sqrt{\frac{2}{\omega\mu\sigma}} \quad (3.36)$$

The grid size from the inner region to the outer region increases until the criteria(3.33).

### 3.4 Numerical Stability

The accuracy and numerical stability are affected by the space increment and time increments used. The accuracy depends on how small the space increments are chosen. To ensure the numerical stability, the time increment  $\Delta t$  must satisfy the Courant stability condition [10]. The classic expression of the Courant stability condition in Cartesian coordinates is given as

$$\Delta t \leq \frac{1}{v \left[ \left( \frac{1}{\Delta x_{min}} \right)^2 + \left( \frac{1}{\Delta y_{min}} \right)^2 + \left( \frac{1}{\Delta z_{min}} \right)^2 \right]} \quad (3.37)$$

where  $\Delta x_{min}$ ,  $\Delta y_{min}$ ,  $\Delta z_{min}$  are the smallest cubic space mesh sizes and  $v$  is the wave velocity in the formation. To achieve stability, the time step  $\Delta t$  is chosen to satisfy the inequality above. In cylindrical coordinates, the above becomes

$$\Delta t = c_f \frac{1}{v \left[ \left( \frac{1}{\Delta \rho_{min}} \right)^2 + \left( \frac{1}{\rho_{min} \Delta \phi_{min}} \right)^2 + \left( \frac{1}{\Delta z_{min}} \right)^2 \right]} \quad (3.38)$$

where  $\Delta \rho_{min}$ ,  $\rho_{min} \Delta \phi_{min}$ ,  $\Delta z_{min}$  are the smallest space grid increments in the cylindrical coordinates, and  $c_f$ (Courant factor) is a parameter less than 1.



## CHAPTER 4

### EXTENSION

#### 4.1 Two Equations-Two Unknown Method

Various applications of FDTD simulations require conversion from time domain data to frequency domain data. The Fast Fourier Transform(FFT) method is traditionally used for the time to frequency domain conversion. However, the FFT method needs a large number of time samples. As an alternative method for single-frequency problems, the Two-Equation Two-Unknown method(2E2U) [11] is implemented here, requiring less time steps than the FFT method. The 2E2U method based on the solution of two linear equations at single frequency(CW) is used to extract amplitude and phase. Assuming a sinusoidal source excitation, the two linear equations are written as

$$\begin{aligned} A \sin(\omega t_1 + \theta) &= q_1 \\ A \sin(\omega t_2 + \theta) &= q_2 \end{aligned} \tag{4.1}$$

where  $A$  and  $\theta$  are the amplitude and phase, and  $\omega$  is the angular frequency. From the FDTD simulations,  $q_1$  and  $q_2$  are obtained at two time steps,  $t_1$  and  $t_2$ . From the two equations above, the two unknowns,  $A$  and  $\theta$ , are obtained as

$$\theta = \arctan \left[ \frac{q_2 \sin(\omega t_1) - q_1 \sin(\omega t_2)}{q_1 \cos(\omega t_2) - q_2 \cos(\omega t_1)} \right] \quad (4.2)$$

$$A = \left| \frac{q_1}{\sin(\omega t_1 + \theta)} \right| \quad (4.3)$$

If  $t_1$  and  $t_2$  are chosen very closely, numerical errors are caused by almost same values of  $q_1$  and  $q_2$ . To choose the proper time steps, the time difference between  $t_1$  and  $t_2$  should be at least one tenth of the period,  $T/10$ . The 2E2U method needs a particular source excitation to obtain more accurate simulation results as discussed next.

## 4.2 Ramped Sine Excitations

The source excitation for the 2E2U method is usually described by a sinusoidal excitation. However, the use of a pure sinusoidal source has two significant problems in the FDTD: DC offset [12] and high frequency contamination [10]. The DC offset is referred to as the nonzero dc component that decays only linearly the time average of a sinusoidal source turned on at  $t = 0$ . The high frequency contamination is related with the discontinuity of the derivation of the source function at  $t = 0$ . For single frequency (CW) problem, a sinusoidal excitation by a ramp function can be used to eliminate the DC offset and the high frequency contamination.

$$v_s = r(t) \sin(\omega t) \quad (4.4)$$

where  $r(t)$ , a raised cosine (RC) ramp function is defined as

$$r(t) = \begin{cases} 0 & t < 0 \\ 0.5[1 - \cos(\frac{\omega t}{2\alpha})] & 0 \leq t \leq \alpha T \\ 1 & t > \alpha T \end{cases} \quad (4.5)$$

where  $T$  is the period of the sine function and  $\alpha$  is a ramp duration parameter (number of sine wave cycles during the ramp duration  $\alpha T$ ). Here, we consider a source with operating frequency  $f = 2$  MHz, and  $\alpha = 0.5$ . For the examples considered, the phase difference and amplitude ratio converge after around  $1.5T$ .

### 4.3 Cylindrical 3-D PML formulation

The FDTD computation domain size is limited by computer memory and CPU time. Ideally, the computational domain should be infinitely large to simulate open region problems, which is not feasible. In this work, a unsplit anisotropic cylindrical perfectly matched layer(PML) [13] is used to simulate the responses of EM logging tools in open regions. The PML acts as an absorber for the electromagnetic fields, so that no spurious reflected fields are produced by the truncated boundaries of the computation domain. Furthermore, the anisotropic medium PML formulations do not modify Maxwell's equations. In 3-D cylindrical coordinates, the PML constitutive tensors related to background constitutive parameters  $\epsilon$ ,  $\mu$  are written as

$$\bar{\epsilon}_{PML} = \epsilon \bar{\Lambda}_{[\rho, \phi, z]}(\rho, z; \omega) \quad (4.6)$$

$$\bar{\mu}_{PML} = \mu \bar{\Lambda}_{[\rho, \phi, z]}(\rho, z; \omega) \quad (4.7)$$

where

$$\bar{\Lambda}_{[\rho, \phi, z]}(\rho, z; \omega) = \phi_\phi \phi_\phi \frac{\rho s_z s_\rho}{\tilde{\rho}} + z_z z_z \frac{\tilde{\rho} s_\rho}{\rho s_z} + \rho_\rho \rho_\rho \frac{\tilde{\rho} s_z}{\rho s_\rho} \quad (4.8)$$

In the above,  $\tilde{\rho}$  is the spatial variable  $\rho$  in the complex variable domain, and  $s_\rho, s_z$  are the frequency-dependent complex stretching variables. The complex coordinate mapping is defined as:

$$\begin{aligned}\rho &\rightarrow \tilde{\rho} = \int_0^\rho s_\rho(\rho') d\rho' \\ &= \int_0^\rho \left( a_\rho(\rho') + i \frac{\Omega_\rho(\rho')}{\omega} \right) d\rho' \\ &= b_\rho(\rho) + i \frac{\Delta_\rho(\rho)}{\omega}\end{aligned}\tag{4.9}$$

$$\begin{aligned}z &\rightarrow \tilde{z} = \int_0^z s_z(z') dz' \\ &= \int_0^z \left( a_z(z') + i \frac{\Omega_z(z')}{\omega} \right) dz' \\ &= b_z(z) + i \frac{\Delta_z(z)}{\omega}\end{aligned}\tag{4.10}$$

where  $a_\rho(\rho)$ ,  $\Omega_\rho(\rho)$ ,  $a_z(z)$ , and  $\Omega_z(z)$  are frequency-independent variables. In addition,  $s_\phi = \tilde{\rho}/\rho$ . Absorption of propagation waves is effected by choosing  $\Omega_z, \Omega_\rho > 0$ . If evanescent modes exit inside PML, one can set  $a_\rho, a_z > 1$  as well. In particular, a PML with  $a_\rho = a_z = 1$  and  $\Omega_\rho = \Omega_z = 0$  becomes the original region. The PML can be extended to match an inhomogeneous medium with constitutive parameters  $\mu$  and  $\epsilon(\mathbf{r}, \omega)$  [14]. The PML constitutive tensors matched to inhomogeneous medium for all frequencies and angles of incidence are simply written as

$$\bar{\epsilon}_{PML} = \epsilon(\mathbf{r}, \omega) \bar{\mathbf{\Lambda}}_{[\rho, \phi, z]}(\rho, z; \omega)\tag{4.11}$$

$$\bar{\mu}_{PML} = \mu \bar{\mathbf{\Lambda}}_{[\rho, \phi, z]}(\rho, z; \omega)\tag{4.12}$$

Note that  $\bar{\mu}_{PML}$  is given in Eq.(4.7). Maxwell's equations are written as

$$i\omega\mu \bar{\Lambda}_{[\rho, \phi, z]} \cdot \mathbf{H} = \nabla \times \mathbf{E} \quad (4.13)$$

$$-i\omega \left(1 + \frac{i\sigma}{\omega\epsilon(\omega)}\right) \epsilon(\omega)\bar{\Lambda}_{[\rho, \phi, z]} \cdot \mathbf{E} = \nabla \times \mathbf{H} \quad (4.14)$$

For a computation convenience, auxiliary fields such as  $\mathbf{H}_a$ ,  $\mathbf{D}_a$ ,  $\mathbf{E}_a$  are defined as

$$\mathbf{H}_a = \bar{\Lambda}_{[\rho, \phi, z]} \cdot \mathbf{H} , \quad \mathbf{D}_a = \bar{\Lambda}_{[\rho, \phi, z]} \cdot \mathbf{D} , \quad \mathbf{E}_a = \bar{\Lambda}_{[\rho, \phi, z]} \cdot \mathbf{E}$$

Eq.(4.13)-(4.14) are rewritten by using the auxiliary fields as

$$\begin{aligned} i\omega\mu\mathbf{H}_a &= \nabla \times \mathbf{E} \\ -i\omega\mathbf{D}_a + \sigma\mathbf{E}_a &= \nabla \times \mathbf{H} \end{aligned} \quad (4.15)$$

The original fields in terms of auxiliary fields are expressed as

$$E_\rho = \frac{s_\rho}{s_\phi s_z} E_{a,\rho} \quad (4.16)$$

$$H_\rho = \frac{s_\rho}{s_\phi s_z} H_{a,\rho} \quad (4.17)$$

$$D_\rho = \frac{s_\rho}{s_\phi s_z} D_{a,\rho} \quad (4.18)$$

Note that the other field components are obtained by cyclic permutation. The above equations replaced by other auxiliary fields such as  $\mathbf{E}_e$ ,  $\mathbf{H}_e$ ,  $\mathbf{D}_e$  can be used to derive first-order differential equations. For example, Eq.(4.16) is given by

$$\begin{aligned}
(i\omega s_\phi)E_{e,\rho} &= (i\omega s_\rho)E_{a,\rho} \\
(i\omega s_z)E_\rho &= i\omega E_{e,\rho}
\end{aligned} \tag{4.19}$$

In the time domain, Eq.(4.19) is written as

$$\begin{aligned}
\left(b_\rho \frac{\partial}{\partial t} + \Delta_\rho\right) E_{e,\rho} &= \left(a_\rho \frac{\partial}{\partial t} + \Omega_\rho\right) E_{a,\rho} \\
\left(a_z \frac{\partial}{\partial t} + \Omega_z\right) E_\rho &= \frac{\partial}{\partial t} E_{e,\rho}
\end{aligned} \tag{4.20}$$

By using a backward differencing scheme, time update equations for the original field in terms of the auxiliary field become

$$\begin{aligned}
(b_\rho + \Delta_\rho \Delta_t) E_{e,\rho}^l &= b_\rho E_{e,\rho}^{l-1} + (a_\rho + \Omega_\rho \Delta_t) E_{a,\rho}^l - a_\rho E_{a,\rho}^{l-1} \\
(a_z + \Omega_z \Delta_t) E_\rho^l &= a_z E_\rho^{l-1} + E_{e,\rho}^l - E_{e,\rho}^{l-1}
\end{aligned} \tag{4.21}$$

By analogy we can use Eq.(4.17) and (4.18) to obtain the remaining update equations. The PML is terminated by a PEC wall at the outer boundary and has a thickness  $d$ . By implementing PML, we need to reduce a reflection error due to the PEC wall and a numerical discretization error due to the abrupt transition of a conductivity profile between the PML and the FDTD discretization. To minimize the reflection error and numerical discretization error, the PML profile increases gradually from the interface of the PML to the PEC outer boundary. Polynomial scaling is chosen as

$$\begin{aligned}
a_\rho &= (\rho/d)^m a_{\rho,max} \\
\Omega_\rho &= 1 + (\Omega_{\rho,max} - 1) \cdot (\rho/d)
\end{aligned} \tag{4.22}$$

Similarly, a polynomial scaling is also used for the  $z$  direction.

## CHAPTER 5

### NUMERICAL SIMULATIONS

#### 5.1 Logging-While-Drilling(LWD) Tool

An electromagnetic well-logging tool is an important part of oil and gas exploration to indicate the formation conductivity at different depths. Logging-While-Drilling(LWD) tool is considered here and has a 4-inch-radius steel mandrel and 5-inch-radius borehole as shown in Figure 5.1. One transmitter and two receivers consist of 4.5-inch-radius wire loop antennas wrapped around the steel mandrel. The two receivers are located at 30 inch and 24 inch away from the transmitter along the LWD tool axis. The transmitter is operated at 2MHz. In the frequency domain, the voltage at the two receivers can be expressed as

$$v_i = FG(L_i), \quad i = 1, 2 \quad (5.1)$$

$$= A_{ri} \angle \theta_{ri} \quad (5.2)$$

where  $F$  is an antenna factor given by the antenna effective lengths and input impedances, and  $G(L_i)$  is the propagation factor by function of  $L_1$  and  $L_2$ , the space



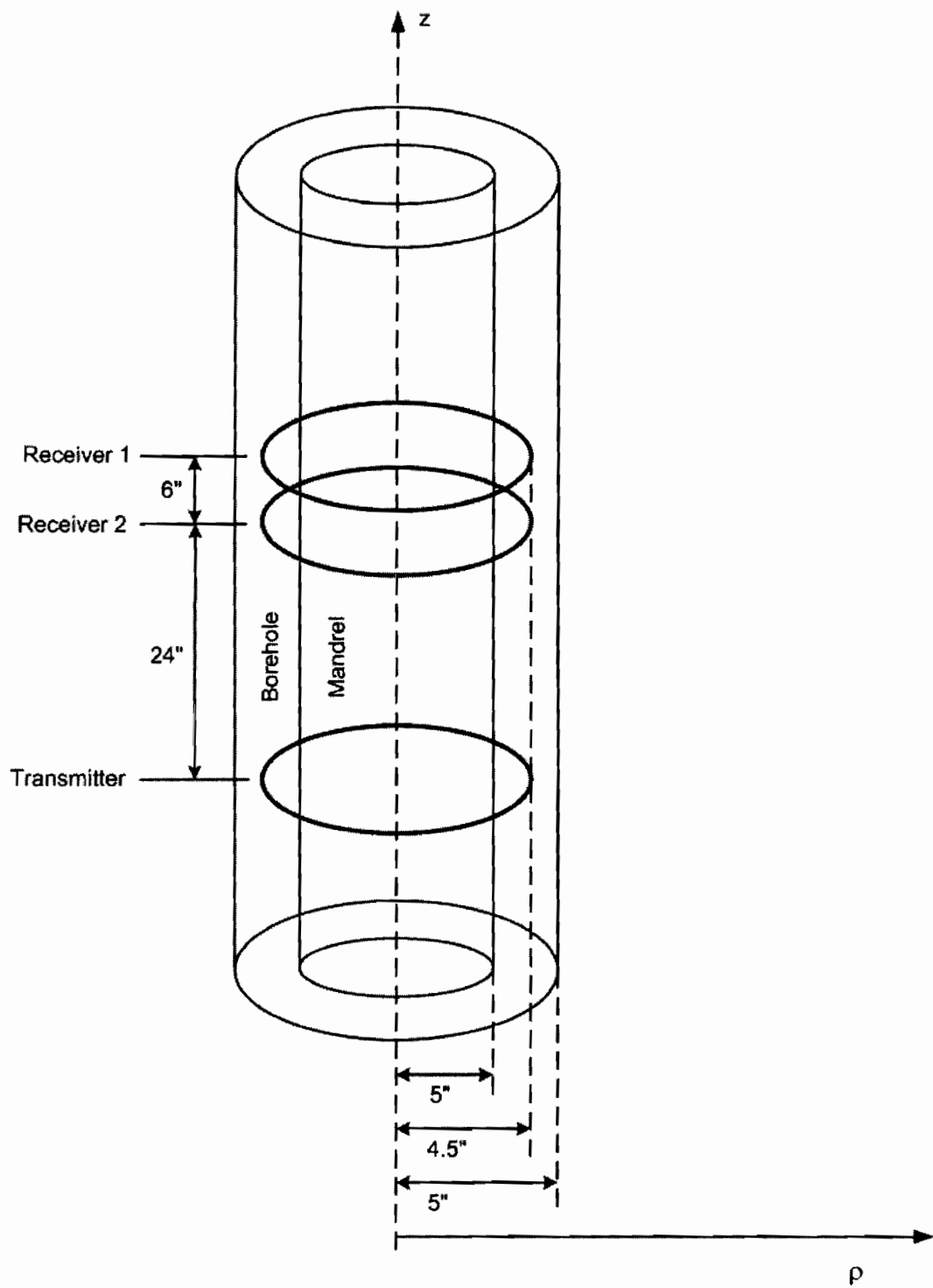


Figure 5.1: The basic structure of the LWD tool

distances between the transmitter and the two receivers, respectively. The antenna factor  $F$  is eliminated to scrutinize the formation outside the LWD tool by taking the voltage ratio as

$$R = \frac{v_1}{v_2} = \frac{G(L_1)}{G(L_2)} \quad (5.3)$$

We are interested in a phase difference(PD) and amplitude ratio(AR) from the above voltage ratio of the formation. The phase difference(PD) and amplitude ratio(AR) are defined as

$$PD = \theta_{r1} - \theta_{r2} \quad (5.4)$$

$$AR = A_{r1}/A_{r2} \quad (5.5)$$

## 5.2 Apparent Resistivity

The resistivity measured by the LWD tool is obtained from the voltage ratio between the two receivers. In an anisotropic formation with an anisotropy ratio  $k$ (Eq.2.2) and oblique angle  $\theta$ , the voltage ratio  $R$  is given as

$$R = \frac{v(L_1, \theta, k, \sigma_h)}{v(L_2, \theta, k, \sigma_h)} \quad (5.6)$$

where the space distances from the transmitter,  $L_1$  and  $L_2$ , are 30 inch and 24 inch, respectively. To calibrate the LWD tool, the same voltage ratio is taken for the LWD tool in air assuming that  $\sigma_h$  and  $\sigma_v$  are equal to 0 to give

$$R_{ah} = \frac{v(L_1, \theta, k, 0)}{v(L_2, \theta, k, 0)} \quad (5.7)$$

Thus, the air calibrated voltage ratio  $R_c$  is defined as

$$R_c = R/R_{ah} \quad (5.8)$$

Alternatively, Eq.(5.8) for phase and amplitude is expressed as

$$\begin{aligned} \phi &= \arg(R_c) \quad (\text{in degree}) \\ A_{dB} &= 20 \log_{10} |R_c| \quad (\text{in dB}) \end{aligned} \quad (5.9)$$

Similarly, the voltage ratio of equivalent homogeneous formation assuming  $k = 1$  (isotropic formation) is given as

$$R_0 = \frac{v(L_1, \theta, 1, \sigma_h)}{v(L_2, \theta, 1, \sigma_h)} \quad (5.10)$$

Also, air calibration applies for the homogeneous voltage ratio of Eq.(5.10). Then, on defining

$$R_{c0} = R_0/R_{ah} \quad (5.11)$$

the homogeneous phase and amplitude are expressed as

$$\begin{aligned}\phi_0 &= \arg(R_{c0}) && (\text{in degree}) \\ A_{dB0} &= 20 \log_{10} |R_{c0}| && (\text{in dB})\end{aligned}\tag{5.12}$$

Apparent phase and amplitude conductivities  $\sigma_{aph}$ ,  $\sigma_{aam}$  are then obtained via interpolation such that

$$y_i = \text{interp}(x, y, x_i) \tag{5.13}$$

where an factor of interest,  $y_i$  is computed for a given  $x_i$  and table of  $[x, y]$  values. Finally, the apparent phase and amplitude resisitivities are obtained by using the the inverse apparent conductivities as,

$$\begin{aligned}R_{aph} &= 1/\text{interp}(\phi_0, \sigma_h, \phi) \\ R_{aam} &= 1/\text{interp}(A_{dB0}, \sigma_h, A_{dB})\end{aligned}\tag{5.14}$$

With tables of  $[\phi_0, \sigma_h]$  and  $[A_{dB0}, \sigma_h]$  for various  $\sigma_h$ .

### 5.3 Discretization

Along the  $\rho$  direction, the region between the 4-in radius steel mandrel and the 5-in radius borehole is discretized using a uniform grid size,  $\Delta\rho = 0.635$  [cm] as shown in Figure 3.3. However, the discretization size  $\Delta\rho$  outside the borehole is nonuniform. The maximum outermost grid size is chosen as  $(\Delta\rho)_{max} = \delta/6$  where the skin depth  $\delta$  for  $\frac{\sigma}{\omega\epsilon} \gg 1$  is given as

$$\delta = \sqrt{\frac{2}{\omega \mu \sigma_{max}}} \quad (5.15)$$

Note that the smallest skin depth  $\delta$  corresponds to the largest conductivity in the formation. In the  $\phi$  direction, the grid size  $\Delta\phi$  is discretized uniformly and chosen via Eq.(3.32) and Eq.(3.33), which is repeated below for convenience

$$\begin{aligned} \Delta l_i &= i \Delta \rho \Delta \phi \\ \Delta l_{max} &\leq \min\left(\frac{\delta}{6}, \frac{\lambda}{10}\right) \end{aligned}$$

Along the  $z$  direction, both the LWD tool geometry and the formation conductivities are considered to decide the discretization size  $\Delta z$ . Here, the discretization size is chosen as uniform,  $\Delta z = 2.54$  cm.

## 5.4 Numerical Results

### 5.4.1 Apparent Resistivity

Figure 5.2 - 5.3 show the apparent resistivities,  $R_{aph}$  and  $R_{aam}$ , versus the anisotropy ratio  $k$  for seven oblique angles  $\theta$  between the anisotropy axis and the LWD tool axis in a homogeneous formation. The domain is discretized by using  $(N_\rho, N_\phi, N_z) = (30, 125, 180)$  in cylindrical coordinates. The nonuniform discretization size  $\Delta\rho$  in  $\rho$  direction varies from 0.635 to 18.7566[cm]. The unsplit field PML in  $z$  direction is set up using 5 cells with a cubic profile for  $a_z, \Omega_z$  at the top and bottom region. The 5-layer PML in  $\rho$  direction employs a cubic profile in the real part of the stretching variables only because the imaginary stretching was found to cause instability

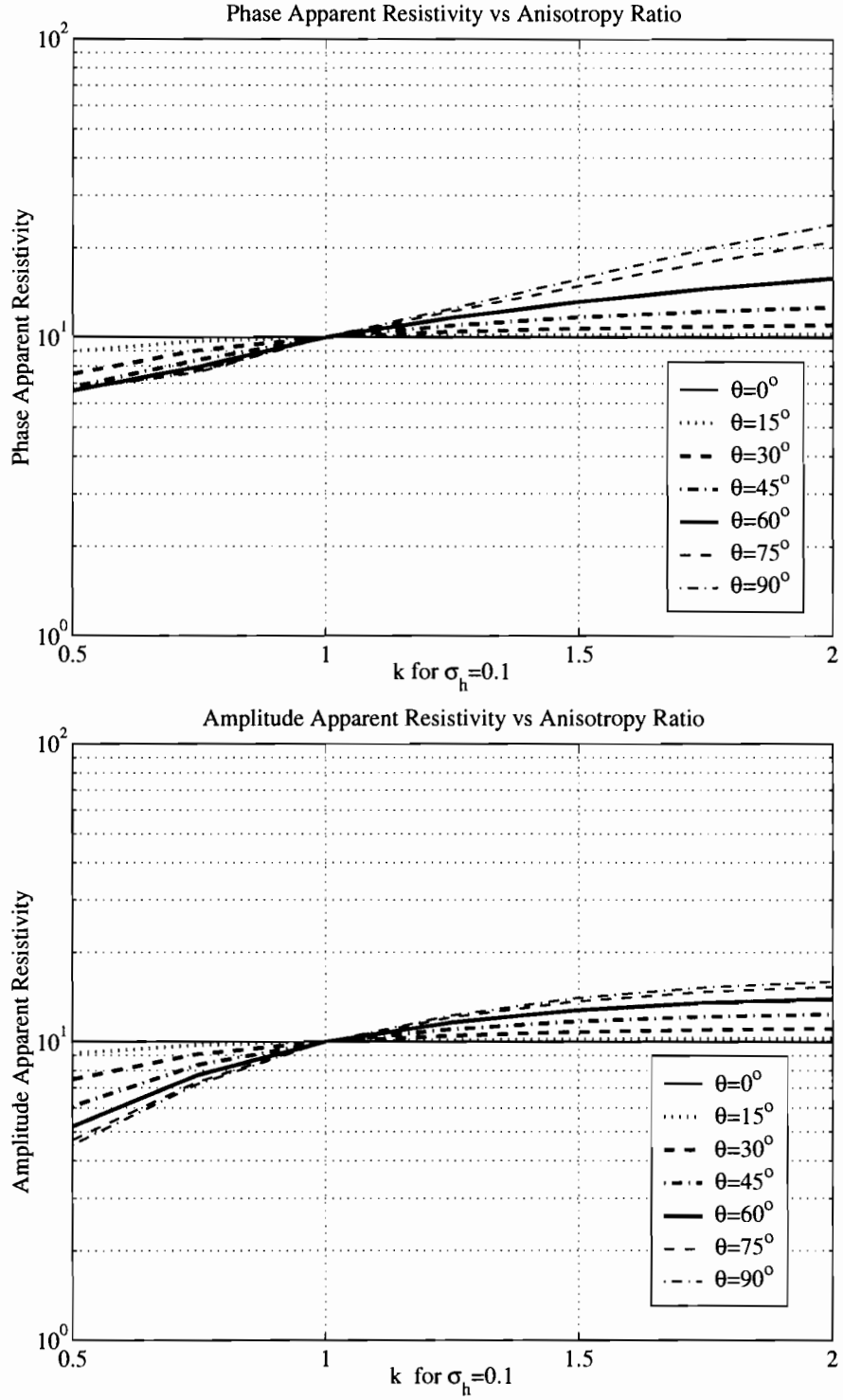


Figure 5.2: Apparent resistivities  $R_{aph}$  and  $R_{aam}$  for  $\sigma_h = 0.1[\text{S/m}]$  without borehole versus anisotropy ratio.

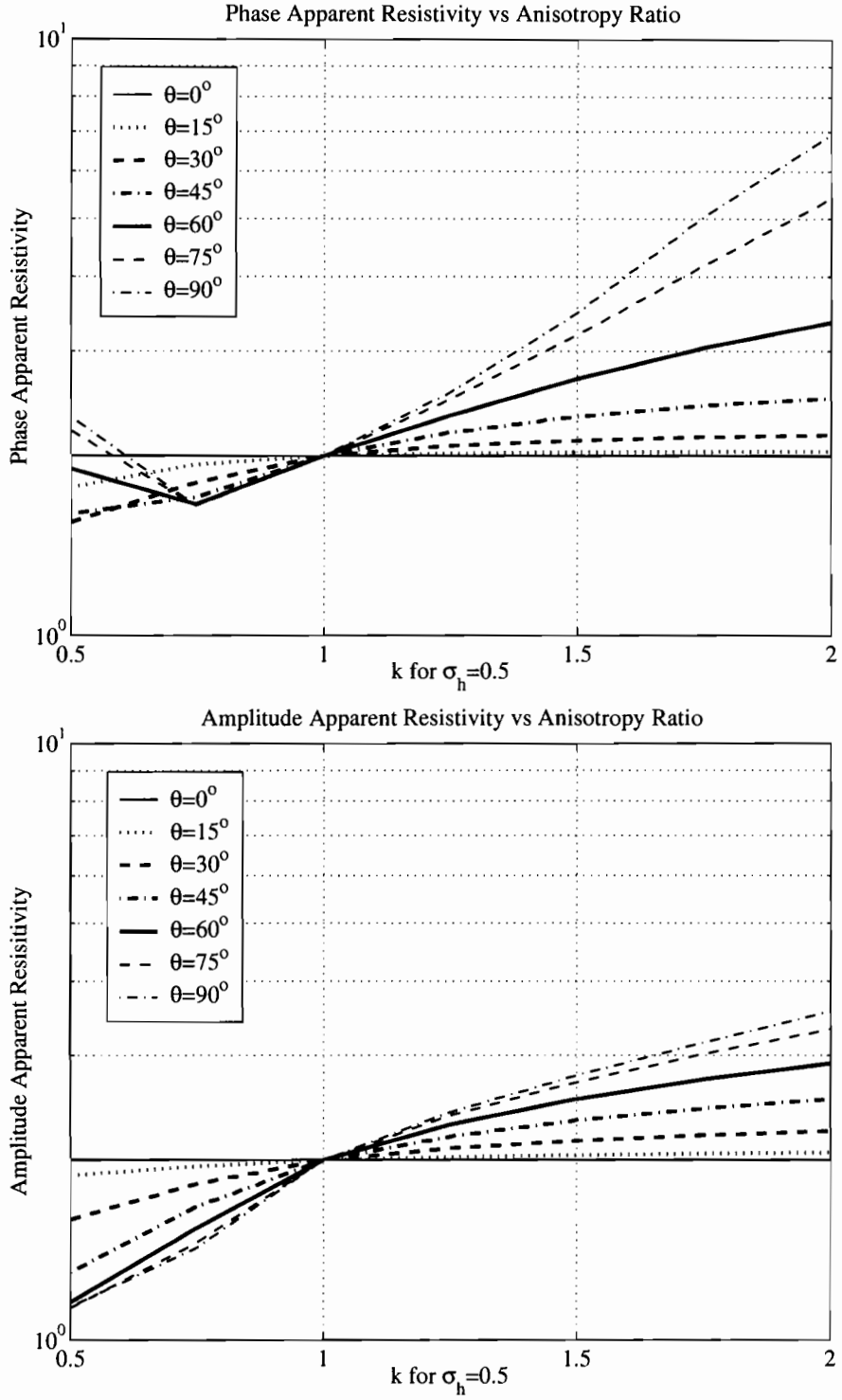


Figure 5.3: Apparent resistivities  $R_{aph}$  and  $R_{aam}$  for  $\sigma_h = 0.5[\text{S/m}]$  without borehole versus anisotropy ratio.

in the full anisotropic case. The relative permittivity and permeability are set to 1. Figure 5.2 and Figure 5.3 show the phase and amplitude apparent resistivities for  $\sigma_h = 0.1$  and  $\sigma_h = 0.5[\text{S/m}]$ , respectively. For  $k = 1$ (the isotropic medium), the apparent resistivities such as  $R_{aph}$  and  $R_{aam}$  for both  $\sigma_h = 0.1$  and  $\sigma_h = 0.5[\text{S/m}]$  cross at  $R_a = R_h (= 1/\sigma_h)$  and are also the same values for various oblique angles. As shown in Figure 5.2 for  $\sigma_h = 0.1[\text{S/m}]$ , both apparent phase and amplitude resistivities increase as  $\sigma_v$  decreases. From Figure 5.3 for  $\sigma_h = 0.5[\text{S/m}]$ , the phase apparent resistivities for  $\theta \geq 60^\circ$  are minimum at  $k = 0.75$ . From these plots, we observe that phase and amplitude apparent resistivities for a general anisotropic medium are sensitive to both  $k$  and  $\theta$ . The results depicted in Figure 5.2- 5.3 show very good agreement with the results of reference [15] using the analytical expressions for Sommerfeld integrals. Therefore, they serve to validate the FDTD algorithm for simulations of a 3-D fully anisotropy tensor in the cylindrical coordinates.

### 5.4.2 Borehole Effect

In the previous section, we have considered a homogeneous formation(no borehole) to compare the analytical results. In practice, a finite radius borehole is present. In this thesis, we consider an oil-based mud and water-based mud with  $\sigma_{mud} = 0.0005$  and  $\sigma_{mud} = 2[\text{S/m}]$ , respectively. Figure 5.4 - 5.6 for  $\sigma_h = 0.5[\text{S/m}]$  show the phase difference and amplitude ratio using no borehole,  $\sigma_{mud} = 0.0005$  and  $\sigma_{mud} = 2[\text{S/m}]$ , respectively. The simulated results for  $\sigma_{mud} = 0.0005$  and  $\sigma_{mud} = 2[\text{S/m}]$  are the same as those without the borehole. Next, Figure 5.7 - 5.8 for  $\sigma_h = 10[\text{S/m}]$  depict the simulated results on  $\sigma_{mud} = 0.0005$  and  $\sigma_{mud} = 2[\text{S/m}]$ , respectively. The discretization size for  $\sigma_h = 10[\text{S/m}]$  is  $(N_\rho, N_\phi, N_z) = (50, 127, 230)$ . The nonuniform grid size



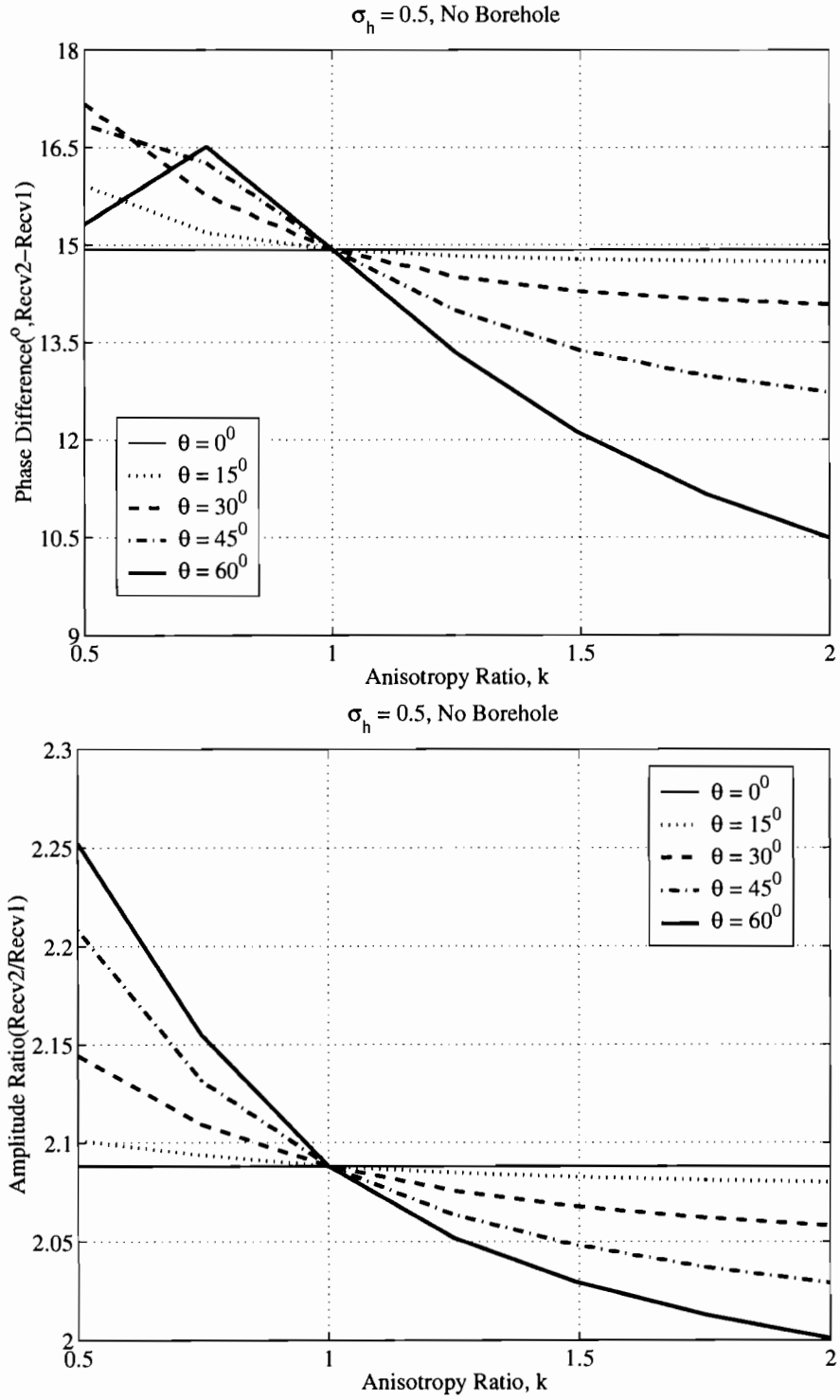


Figure 5.4: Phase Difference and Amplitude Ratio versus anisotropy ratio for  $\sigma_h = 0.5$ [S/m] without Borehole.

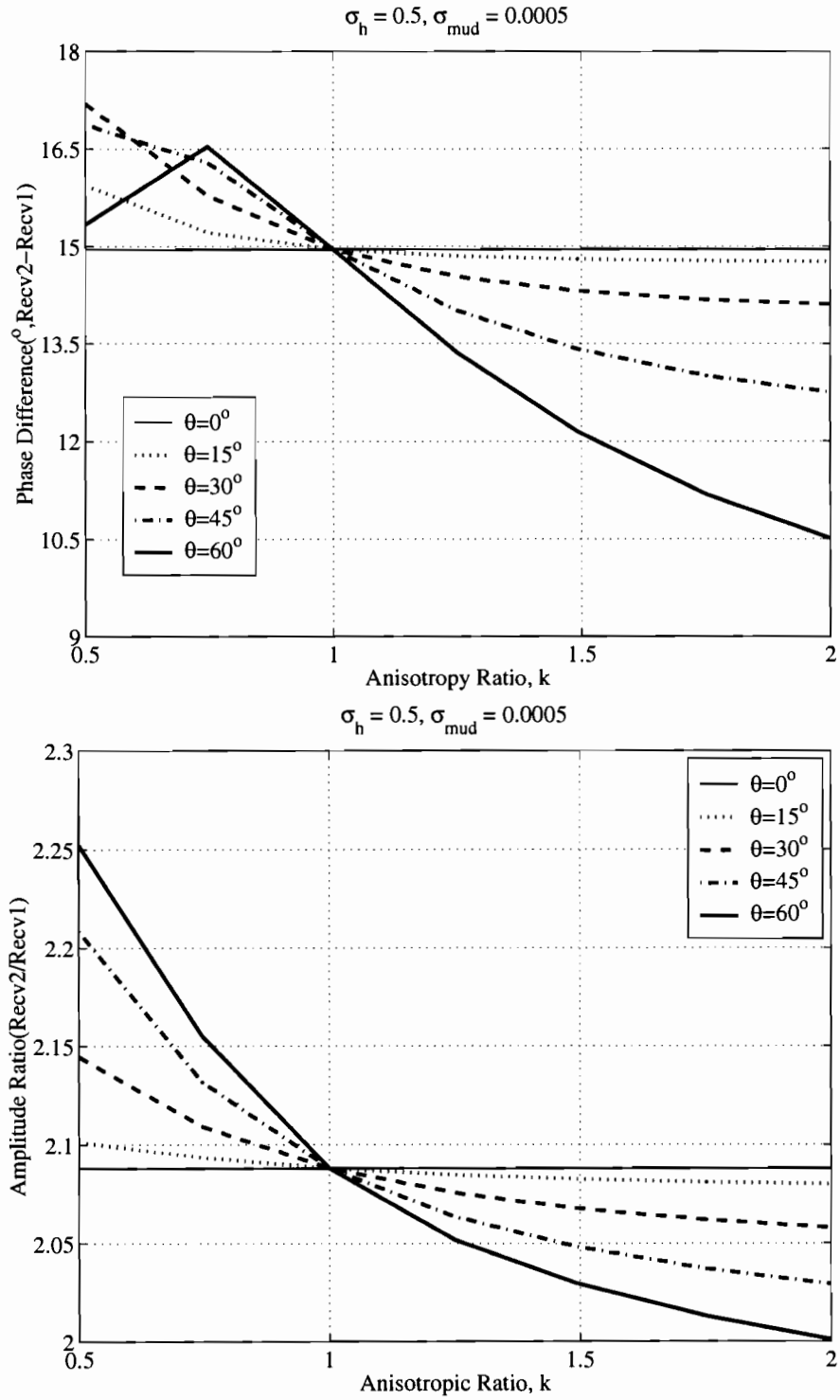


Figure 5.5: Phase Difference and Amplitude Ratio versus anisotropy ratio for  $\sigma_h = 0.5[\text{S/m}]$  with  $\sigma_{mud} = 0.0005[\text{S/m}]$ .

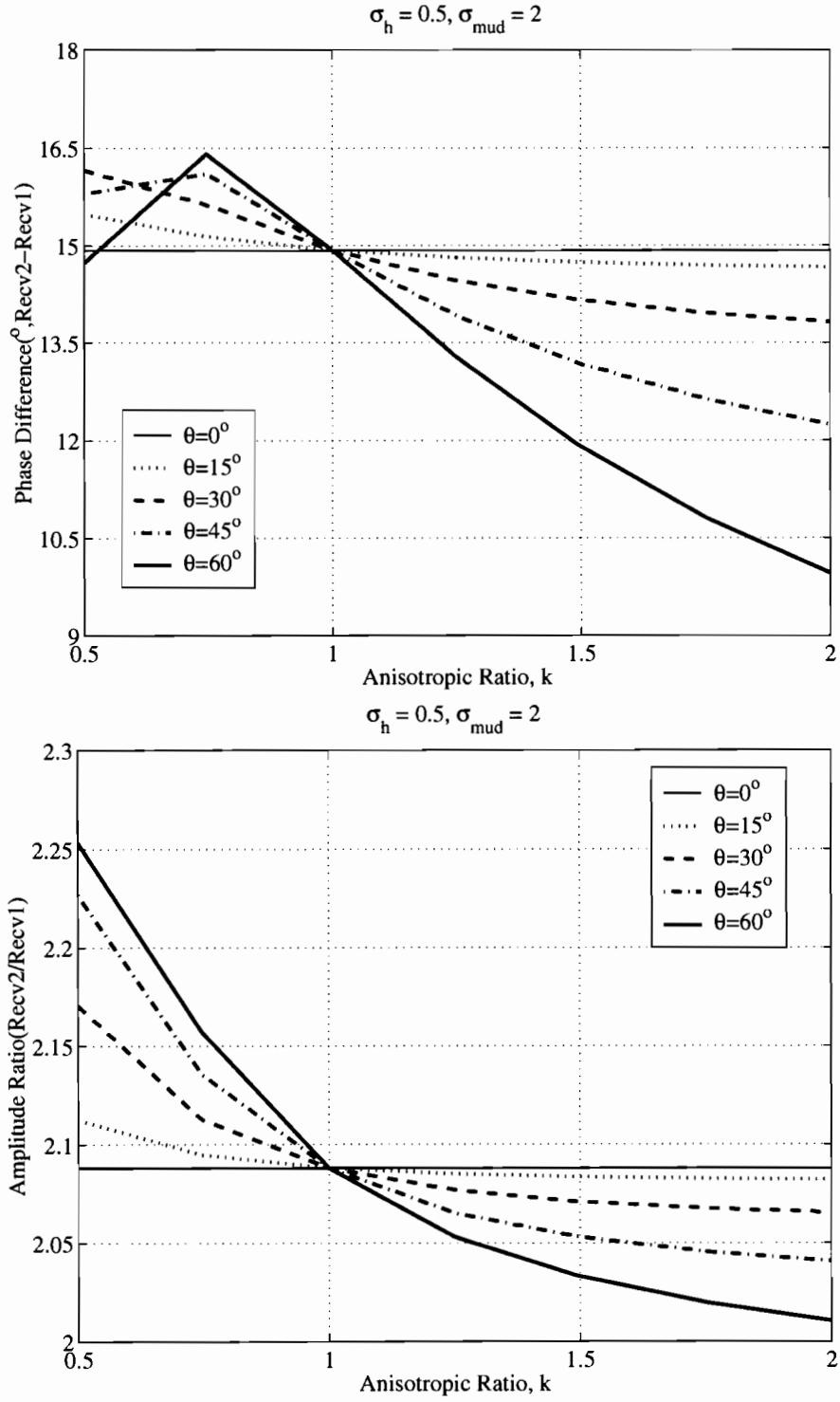


Figure 5.6: Phase Difference and Amplitude Ratio versus anisotropy ratio for  $\sigma_h = 0.5[\text{S/m}]$  with  $\sigma_{mud} = 2[\text{S/m}]$ .

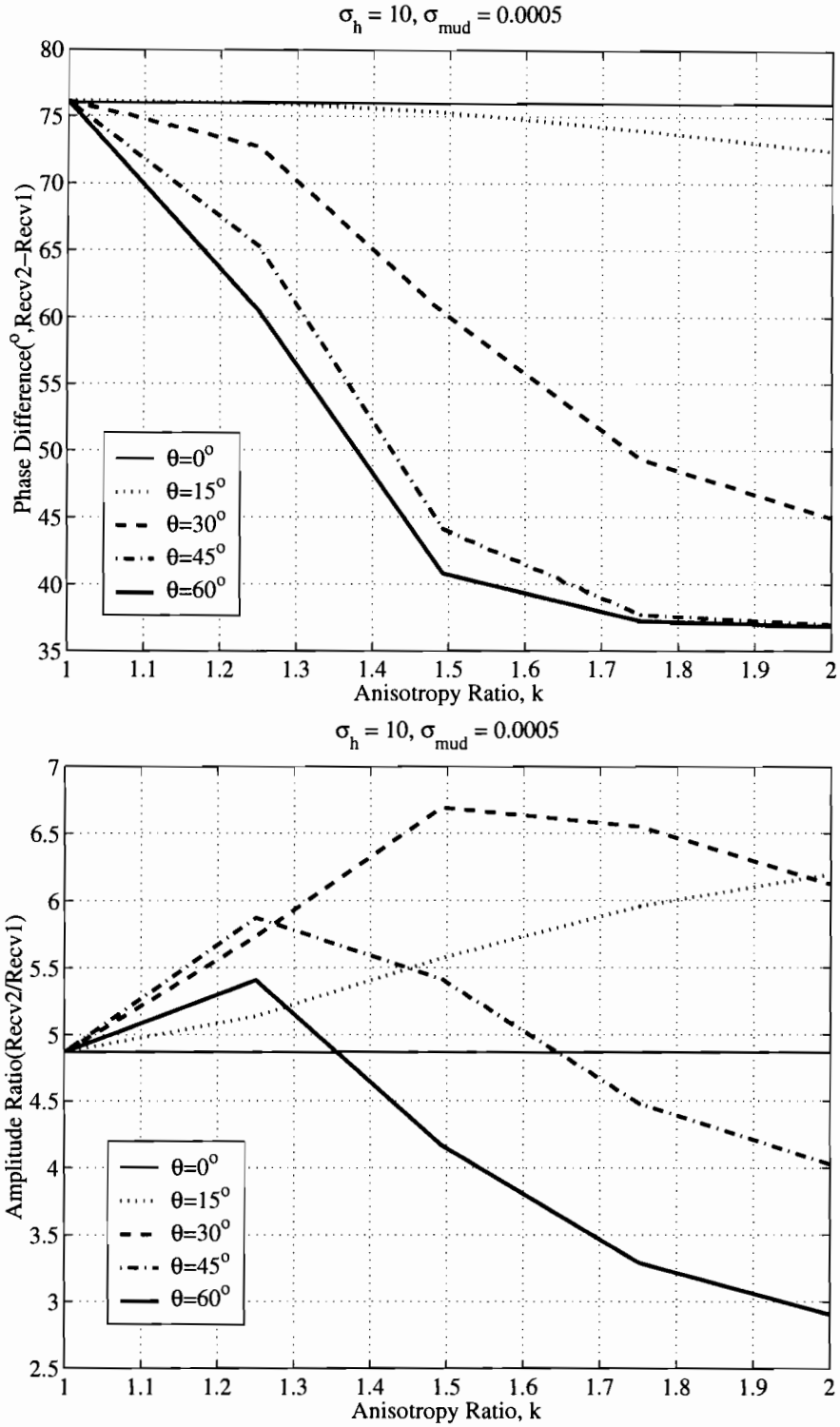


Figure 5.7: Phase Difference and Amplitude Ratio versus anisotropy ratio for  $\sigma_h = 10[\text{S/m}]$  with  $\sigma_{mud} = 0.0005[\text{S/m}]$ .

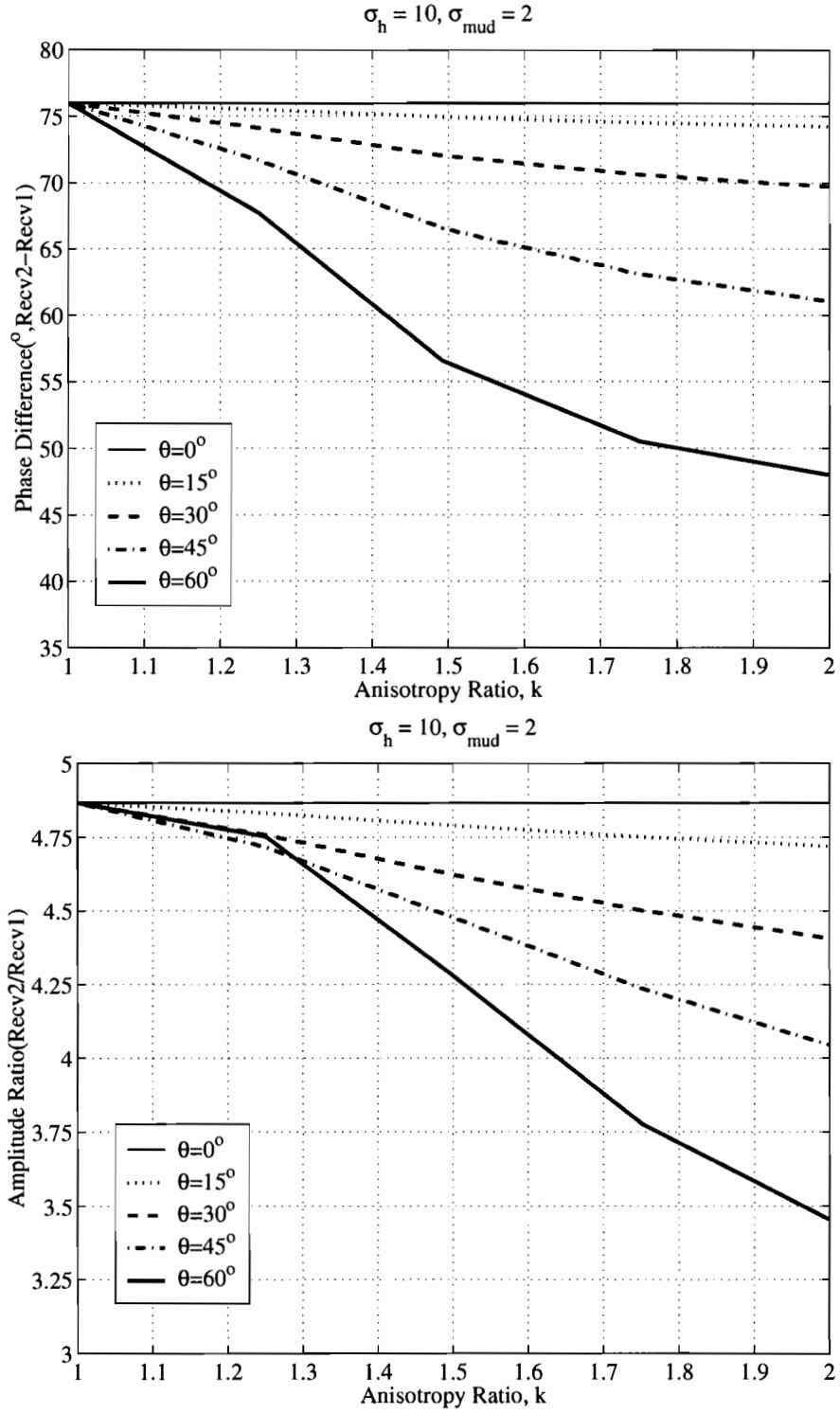


Figure 5.8: Phase Difference and Amplitude Ratio versus anisotropy ratio for  $\sigma_h = 10$ [S/m] with  $\sigma_{mud} = 2$ [S/m].

increases from 0.635 to 1.8757[cm]. We consider that the range of the anisotropy ratio is from  $k = 1$  to 2 because a horizontal conductivity of the earth surface is often larger than a vertical conductivity [16]. From Figure 5.7 for  $\sigma_{mud} = 0.0005[\text{S/m}]$ , the results of the phase difference are smaller for larger  $k$  and for  $\theta \geq 45^\circ$  are close in behavior. The results of the amplitude ratio show a non-monotonic behavior. However, the phase difference and amplitude ratio using  $\sigma_{mud} = 2[\text{S/m}]$  decrease for both  $k$  and  $\theta$ . From the observations, results with low  $\sigma_h$  are not affected by  $\sigma_{mud}$  while the simulations of high  $\sigma_h$  are very sensitive to  $\sigma_{mud}$ .

### 5.4.3 Anisotropic Dipping Bed (True Vertical Thickness)

Figure 5.9 illustrates a 3-layer inhomogeneous formation with an anisotropic dipping bed(true vertical thickness) for various dipping angles. The true vertical thickness is retrieved as the original thickness(60inch) for all dipping angles. The upper and lower layers have an isotropy conductivity  $\sigma_{iso}$  whereas the middle layer as the dipping bed has an anisotropy tensor with a horizontal conductivity  $\sigma_h$  and vertical conductivity  $\sigma_v$ . The conductivity of mud used in LWD tool is chosen as  $\sigma_{mud} = 0.0005[\text{S/m}]$  for the oil-based mud and  $\sigma_{mud} = 2[\text{S/m}]$  for the water-based mud. Let the first intersection point of the lower layer and the dipping bed be Point1. Similarly, the intersection point of the dipping bed and the upper layer is Point2(see Figure 5.9). The domain is discretized by using  $(N_\rho, N_\phi, N_z) = (50, 127, 230)$ . The grid size in the  $z$  direction is  $\Delta z = 2.54[\text{cm}]$ . In  $\rho$  direction, the discretization size  $\Delta \rho$  increases nonuniformly from 0.635 to 1.8757[cm]. The maximum grid size is chosen by the skin depth of the largest conductivity in the formation. The PML in  $\rho$  direction is set up by using 5 cells and a cubic profile on the real part only of the stretching variables

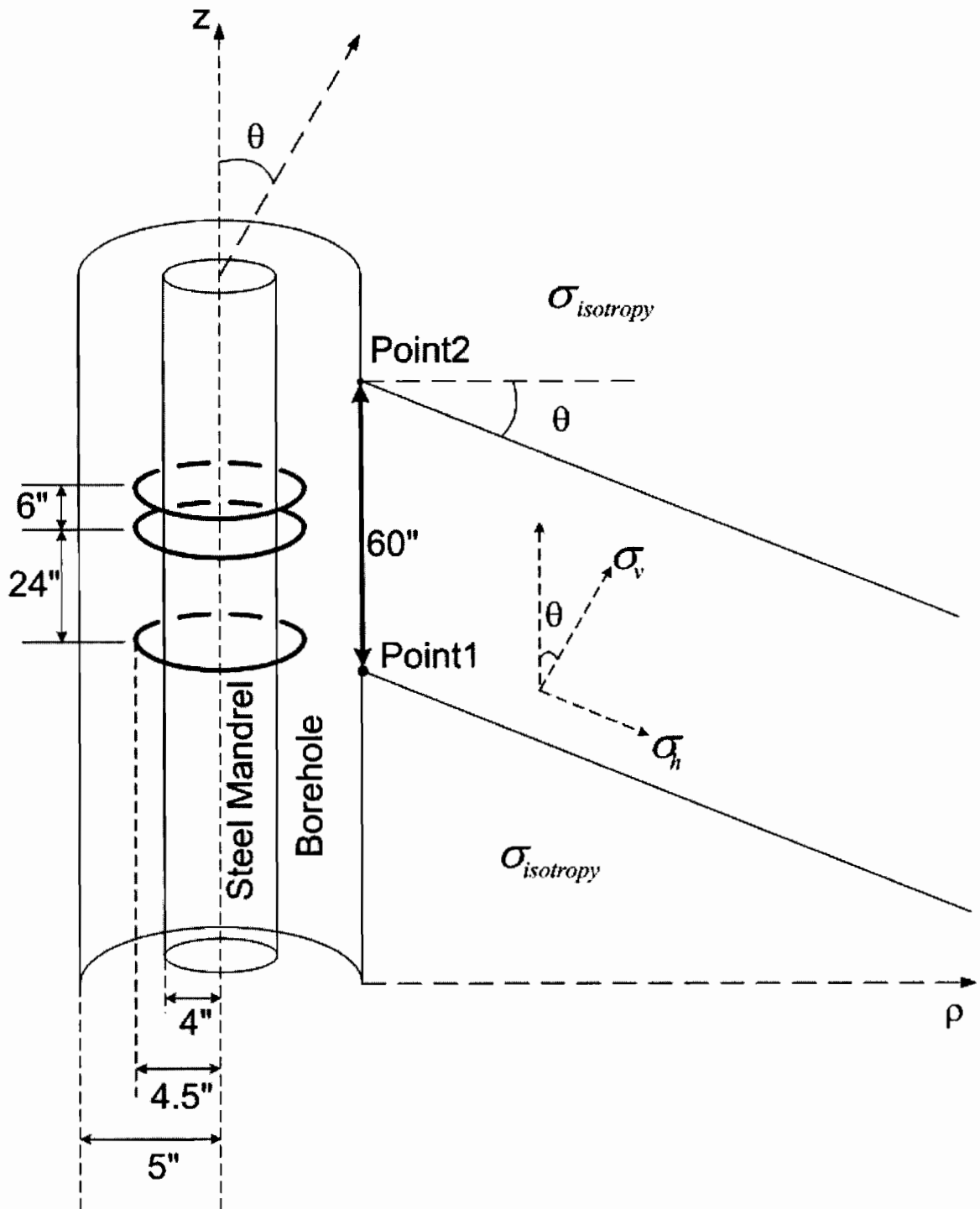


Figure 5.9: Illustration of the LWD tool and a 3-layer formation with a true vertical thickness of dipping bed

to avoid instability due to the imaginary part. A 5-cell PML in  $z$  direction employs a cubic profile on both real and imaginary parts.

### A. Effect of Horizontal and Vertical Conductivities

In this section, the LWD tool is simulated to study the effect of horizontal or vertical elements of an anisotropy conductivity tensor. The formation illustrated in Figure 5.9 for the vertical case,  $\theta = 0^\circ$ , has the three layers where the upper and lower layers conductivities have the identity tensor with  $\sigma_{iso} = 10[\text{S/m}]$ . For the middle layer, the conductivities of  $\sigma_h$  and  $\sigma_v$  are chosen to be 2.5 or 0.5[S/m] in three different combinations. The conductivity of the mud is  $\sigma_{mud} = 2[\text{S/m}]$ . As shown in Figure 5.10, the phase difference and amplitude ratio for  $\sigma_h = 2.5$  and  $\sigma_v = 2.5[\text{S/m}]$  are exactly the same as those for  $\sigma_h = 2.5$  and  $\sigma_v = 0.5[\text{S/m}]$ . However, the results for  $\sigma_h = 0.5$  and  $\sigma_v = 0.5[\text{S/m}]$  are obviously different. Therefore, we conclude, as expected, that for the vertical case,  $\theta = 0^\circ$ , the response of the LWD tool is controlled only by the horizontal conductivity  $\sigma_h$ .

### B. Dipping Angle Effects

In this section, we examine effect of a dipping bed according to a dipping angle without anisotropy. The responses of the LWD tool are simulated in a 3-layer formation with an isotropic dipping bed. The identity tensor of the isotropic conductivity has  $\sigma_h = \sigma_v = 2.5 [\text{S/m}]$  for various dipping angles. The lower and upper layers have  $\sigma_{iso} = 10 [\text{S/m}]$ . The conductivity of the mud is  $\sigma_{mud} = 2[\text{S/m}]$ . Figure 5.11 shows the phase difference and amplitude ratio of the LWD tool for  $\theta = 0^\circ, 45^\circ$  and  $60^\circ$ . When the receiver1 is located close to the interface between layers, the phase difference and amplitude ratio change abruptly. The transition at these interfaces



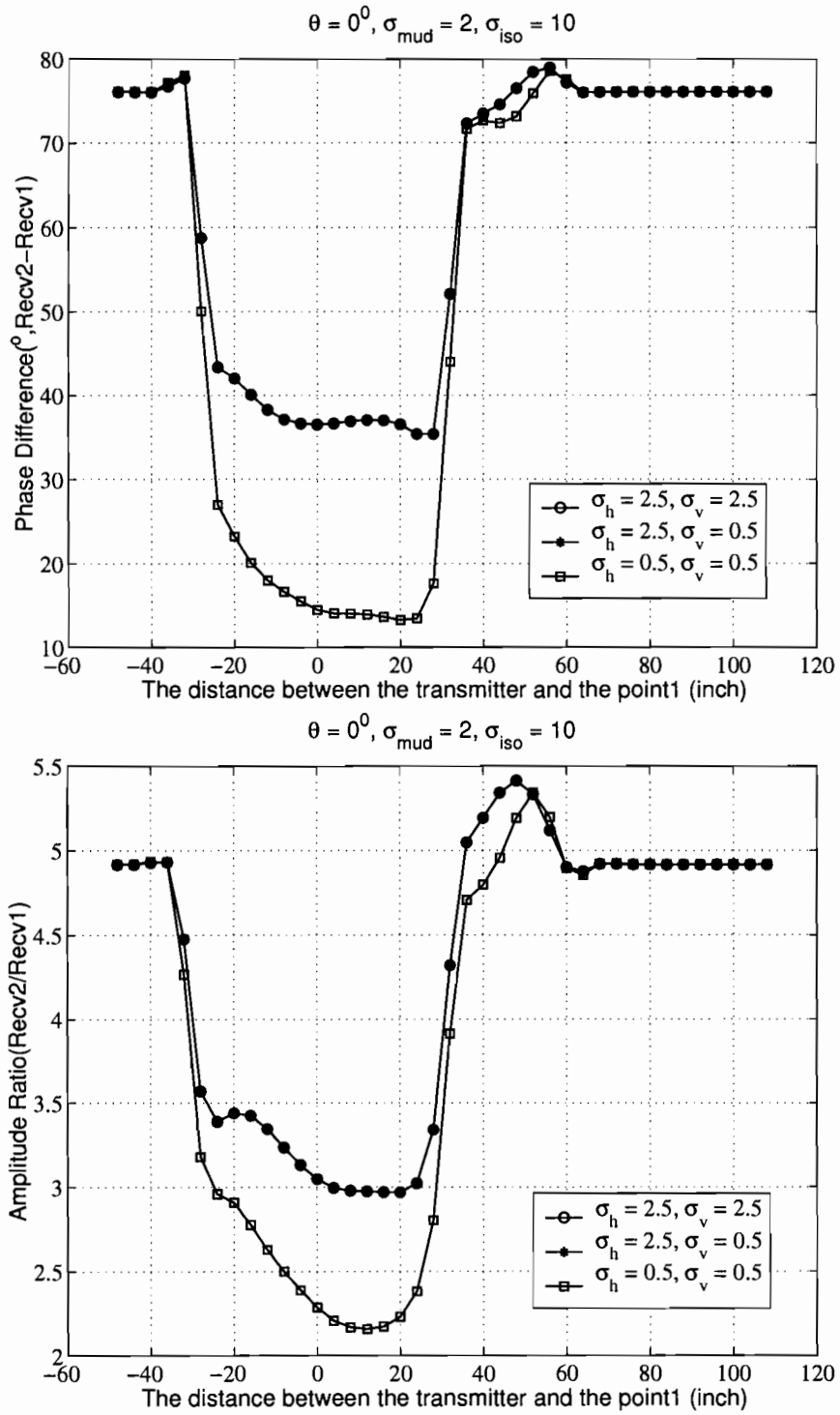


Figure 5.10: The effect of the horizontal conductivity in an inhomogeneous anisotropic dipping bed.

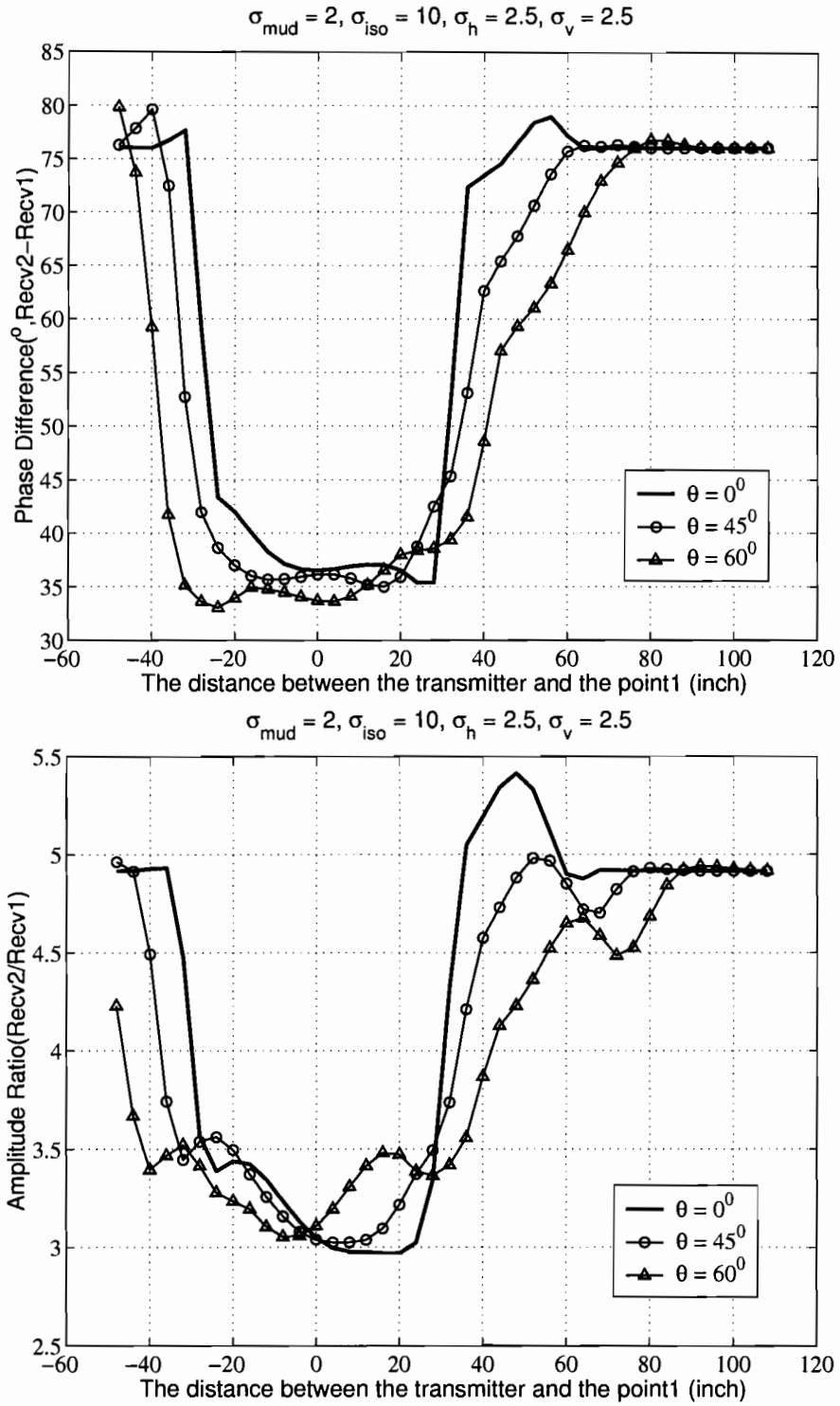


Figure 5.11: Simulation results of the LWD in an inhomogeneous isotropic dipping bed.

depends on the skin depth  $\delta$  in the formation. As the dipping angle increases, the shoulder effect is less because of the slower transition at Point1 and Point2. When the receiver1 reaches the middle of the dipping bed, the phase difference and amplitude ratio for various dipping angles approach  $35^\circ$  and 3.1, corresponding to Figure A.2 with an equivalent thick bed. The behavior according to the dipping angle is similar to reference [17].

### C. Anisotropic Dipping Bed (True Vertical Thickness)

As depicted in Figure 5.9, we next simulate the results for phase difference and amplitude ratio of the LWD tool penetrating a three-layer formation with an 60-inch anisotropy dipping bed(true vertical thickness) for seven dipping angles. Figure 5.12 shows simulated results when  $\sigma_h$ ,  $\sigma_v$ , and  $\sigma_{iso}$  are chosen to be 2.5, 0.5, 10[S/m], respectively. The conductivity of the mud is  $\sigma_{mud} = 2$ [S/m]. When the receiver1 approaches Point1 and Point2, the apparent thickness of the anisotropic dipping bed is wider because of the outward slower transition due to the high  $\sigma_{iso}$  as the dipping angle increases. Comparing the behavior for  $\theta = 60^\circ$  shown in Figure 5.11, the horns at the interfaces are clearly observed and the horn effect increases for the higher dipping angle. In the region of the anisotropy dipping bed, the phase difference and amplitude ratio are less than the results of the isotropic bed with  $\sigma_h = \sigma_v = 2.5$ [S/m] as shown in Figure 5.9. When two receivers and the transmitter pass through completely the dipping bed, the phase difference and amplitude ratio converge to the phase difference and amplitude ratio of the conductivity of the isotropic layer(Figure A.2). Figure 5.13 depicts the simulation results of the same formation with  $\sigma_{mud} = 0.0005$  instead of  $\sigma_{mud} = 2$ [S/m]. The overall characteristics for  $\sigma_{mud} = 0.0005$ [S/m] are not much different from those for  $\sigma_{mud} = 2$ [S/m], but the results using  $\sigma_{mud} = 0.0005$ [S/m] are

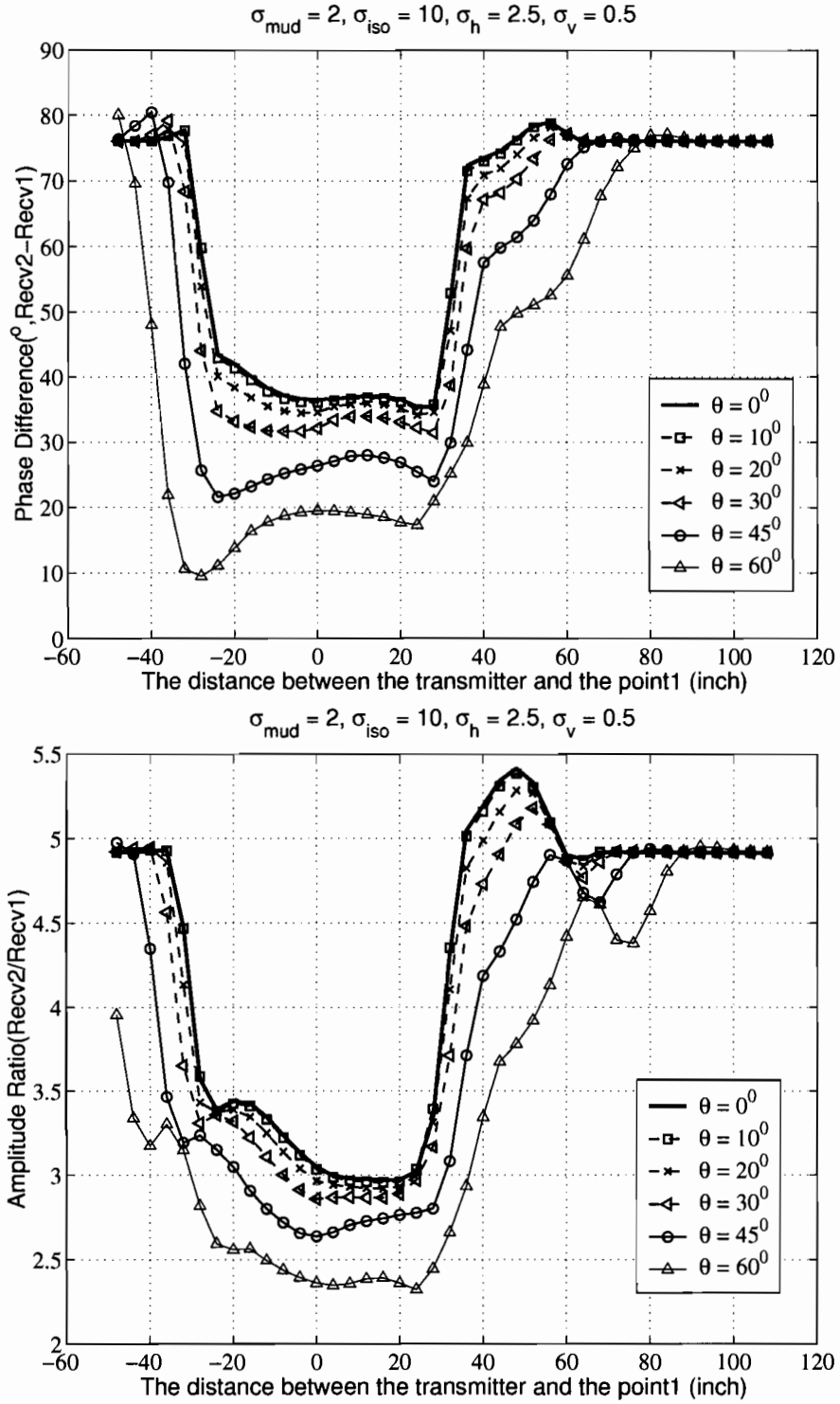


Figure 5.12: Simulation results of the LWD tool using  $\sigma_{mud} = 2[\text{S/m}]$  crossing an inhomogeneous anisotropic dipping bed with  $\sigma_h = 2.5$ ,  $\sigma_v = 0.5$ , and  $\sigma_{iso} = 10[\text{S/m}]$ . (True vertical thickness)

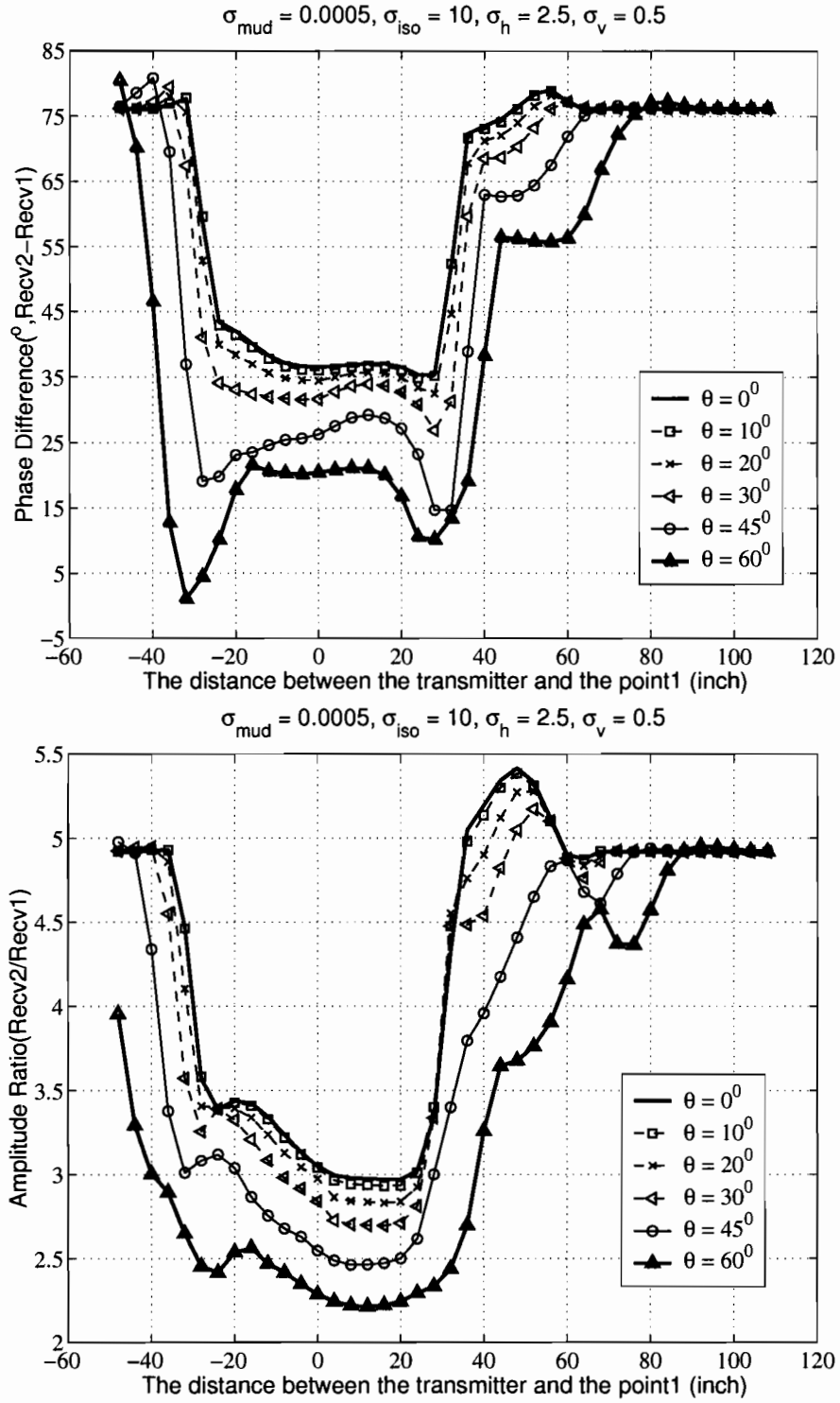


Figure 5.13: Simulation of the LWD using  $\sigma_{mud} = 0.0005[\text{S/m}]$  crossing an inhomogeneous anisotropy dipping bed with  $\sigma_h = 2.5$ ,  $\sigma_v = 0.5$ , and  $\sigma_{iso} = 10[\text{S/m}]$ . (True vertical thickness)

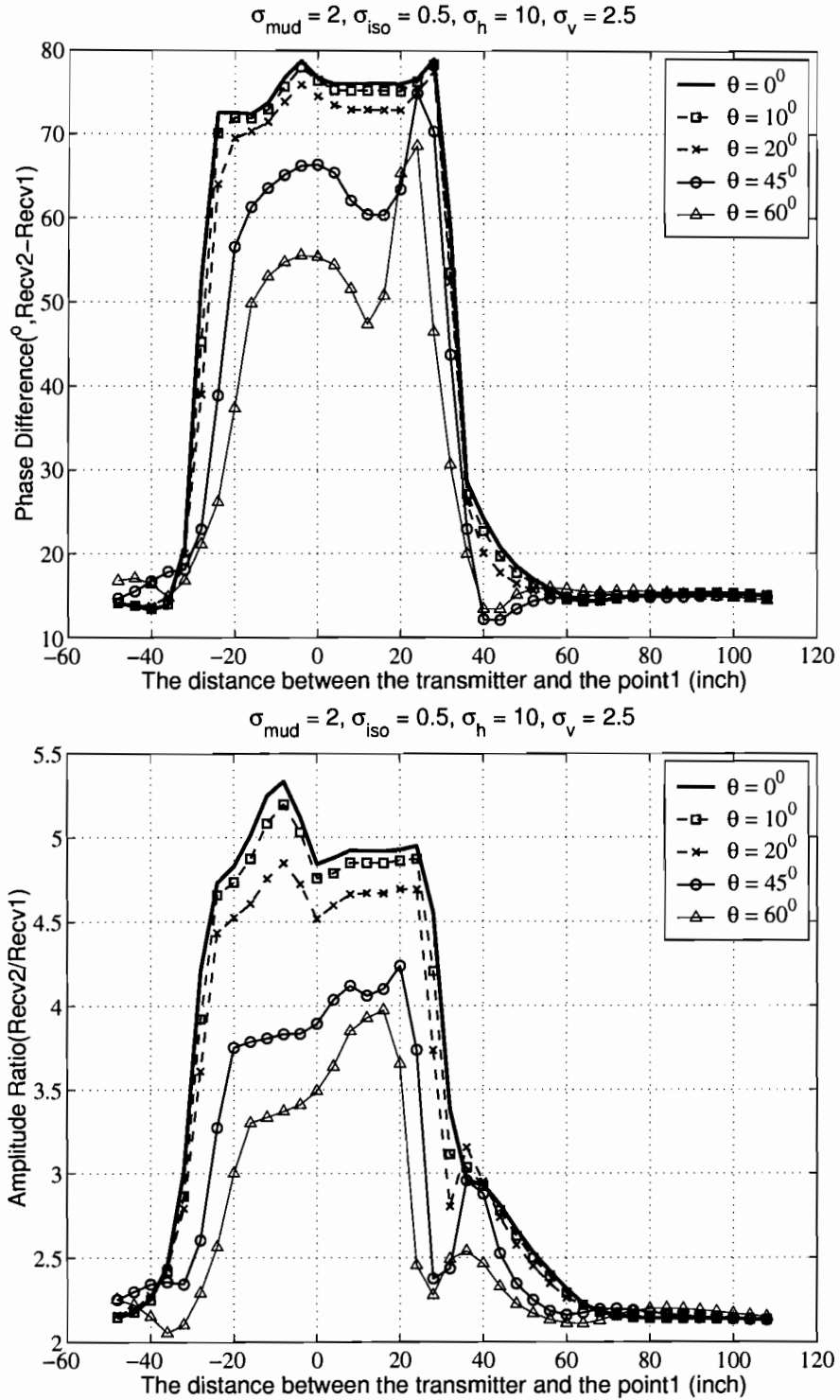


Figure 5.14: Simulation of the LWD tool using  $\sigma_{mud} = 2[\text{S/m}]$  crossing an inhomogeneous anisotropic dipping bed with  $\sigma_h = 10$ ,  $\sigma_v = 2.5$ , and  $\sigma_{iso} = 0.5[\text{S/m}]$ . (True vertical thickness)

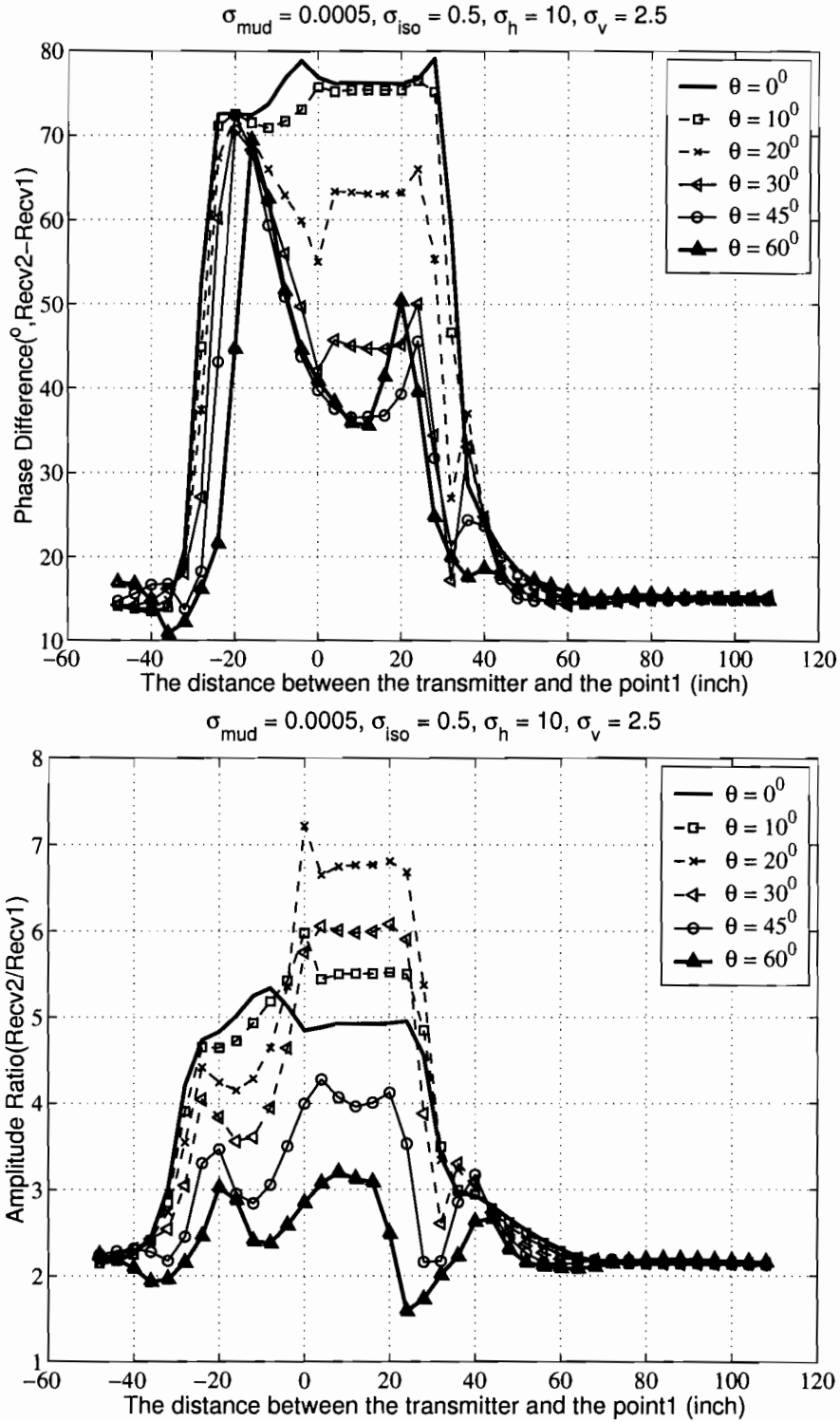


Figure 5.15: Simulation of the LWD tool using  $\sigma_{mud} = 0.0005[\text{S/m}]$  crossing an inhomogeneous anisotropic dipping bed with  $\sigma_h = 10$ ,  $\sigma_v = 2.5$ , and  $\sigma_{iso} = 0.5[\text{S/m}]$ . (True vertical thickness)

slightly smaller than those of  $\sigma_{mud} = 2$  [S/m] when the receiver1 approaches Point1 and Point2. Hence, the horn effect of  $\sigma_{mud} = 2$  is less pronounced than that of  $\sigma_{mud} = 2$ [S/m].

Next, Figure 5.14 and 5.15 show the simulation results with  $\sigma_{iso} = 0.5$ ,  $\sigma_h = 10$  and  $\sigma_v = 2.5$ [S/m], respectively. In Figure 5.14 and Figure 5.15, the conductivities of mud are used by  $\sigma_{mud} = 2$  and  $\sigma_{mud} = 0.0005$ [S/m], respectively. In both cases, the phase difference and amplitude ratio vary abruptly at Point1 and Point2 due to the large conductivity  $\sigma_h = 10$ [S/m]. As the dipping angle increases, the apparent thickness is reduced because the inward transition due to low  $\sigma_{iso}$  is less abrupt. As the receiver1 reaches at the middle of the anisotropic dipping bed, Figure 5.14 for  $\sigma_{mud} = 2$ [S/m] shows that phase difference and amplitude ratio are reduced as expected from Figure 5.8. From Figure 5.15 with  $\sigma_{mud} = 0.0005$ [S/m], the phase difference with the larger dipping angle than  $45^\circ$  are similar while the amplitude ratio changes considerably, as expected from Figure 5.7. Comparing Figure 5.12-5.13 and Figure 5.14- 5.15, we observe that the effect of  $\sigma_{mud}$  on the LWD tool is more significant when  $\sigma_h$  is larger. For larger dipping angles, it becomes more difficult to determine high conductive values on dipping beds by LWD tools using the water-based mud because the phase difference and the amplitude ratio for the higher dipping angles show more complex behaviors.

#### 5.4.4 Anisotropic Dipping Bed (Actual Thickness)

Figure 5.16 illustrates a 3-layer inhomogeneous formation including an anisotropic dipping bed with an actual thickness for various dipping angles. The actual thickness according to being equal to 60[inch] for  $\theta = 0^\circ$  varies in proportion to  $1/\cos\theta$  for



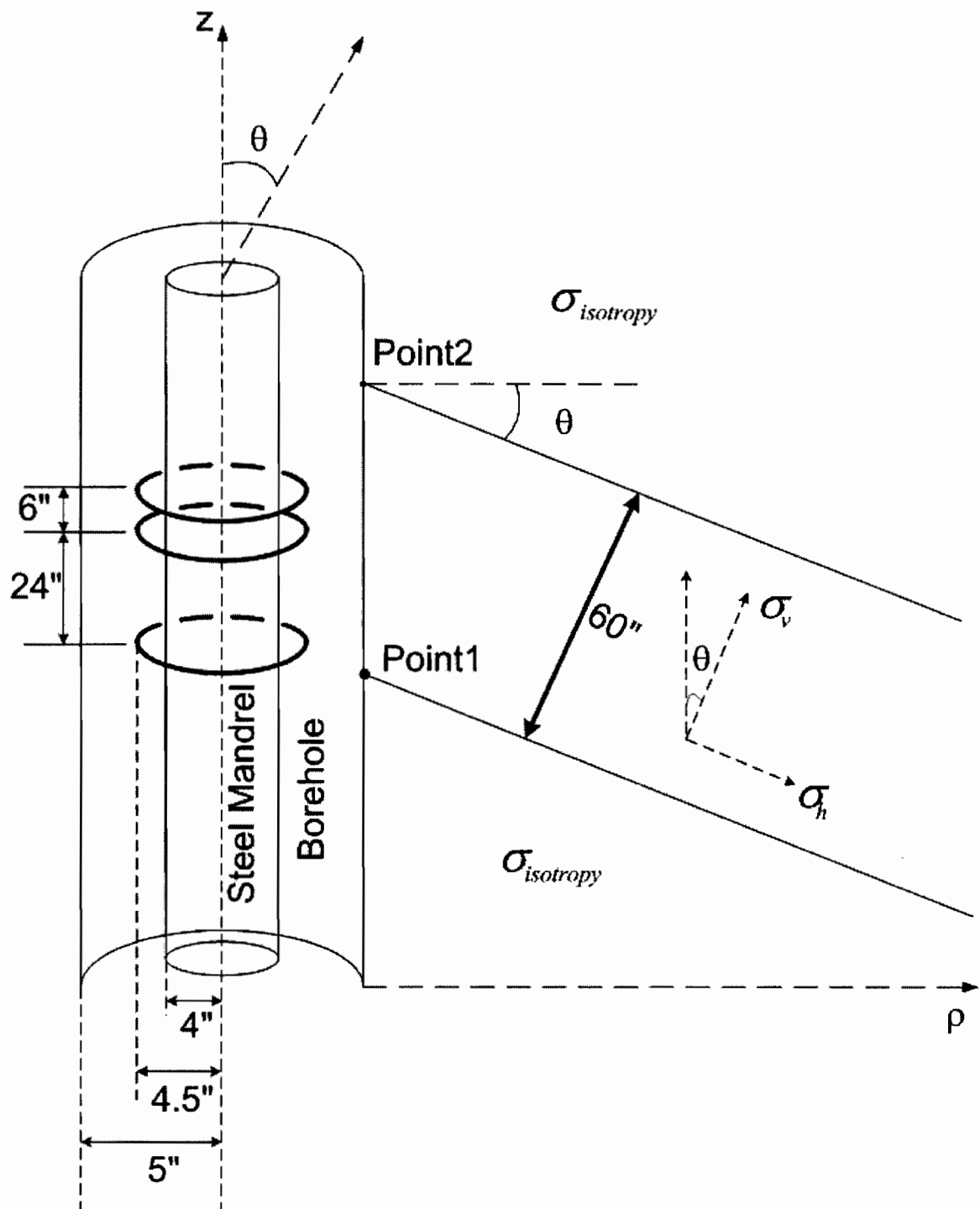


Figure 5.16: Illustration of the LWD tool and a 3-layer formation with a actual thickness

the dipping angles. Figure 5.17- 5.18 show the results in the formation with  $\sigma_h = 2.5$ ,  $\sigma_v = 0.5$  and  $\sigma_{iso} = 10$ [S/m]. The conductivities of mud for Figure 5.17- 5.18 are  $\sigma_{mud} = 2$ ,  $\sigma_{mud} = 0.0005$ [S/m], respectively. Comparing Figure 5.12- 5.13 and Figure 5.17- 5.18, the overall behaviors are similar. As the dipping angle is higher, the center region is much wider due to the effect of the actual thickness and the horn effect is less observed. Next, Figure 5.19 and Figure 5.20 show the results with  $\sigma_h = 10$ ,  $\sigma_v = 2.5$  and  $\sigma_{iso} = 0.5$ [S/m], respectively. The conductivities of mud are  $\sigma_{mud} = 2$ ,  $\sigma_{mud} = 0.0005$ [S/m], respectively. For the higher dipping angle, the center region shown in Figure 5.19 and 5.20 tends to be large due to the effect of the actual thickness while the center region shown in Figure 5.14- 5.15 is narrow due to inward transition at the interfaces.

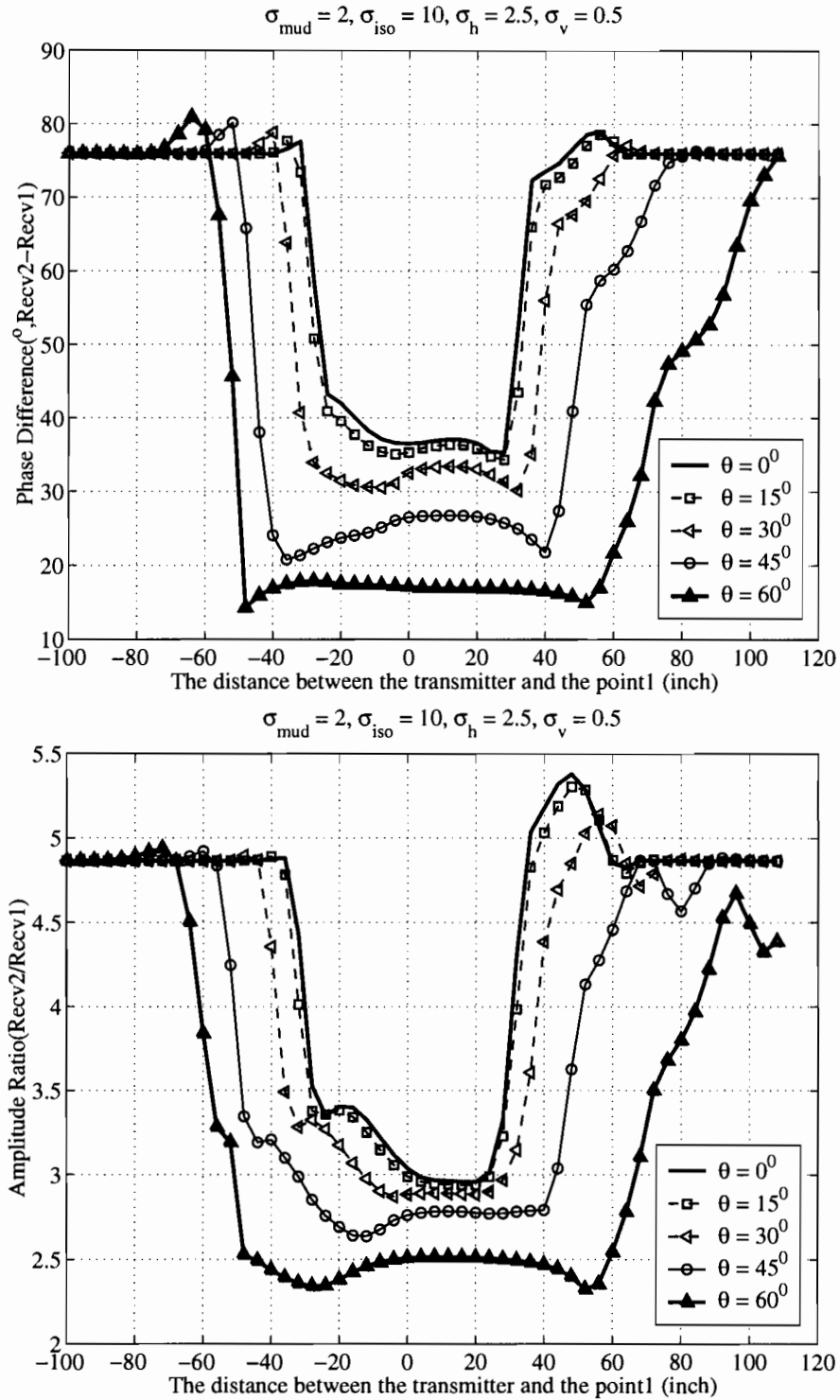


Figure 5.17: Simulation results of the LWD tool using  $\sigma_{mud} = 2[\text{S/m}]$  crossing an inhomogeneous anisotropic dipping bed with  $\sigma_h = 2.5$ ,  $\sigma_v = 0.5$ , and  $\sigma_{iso} = 10[\text{S/m}]$ (Actual thickness).

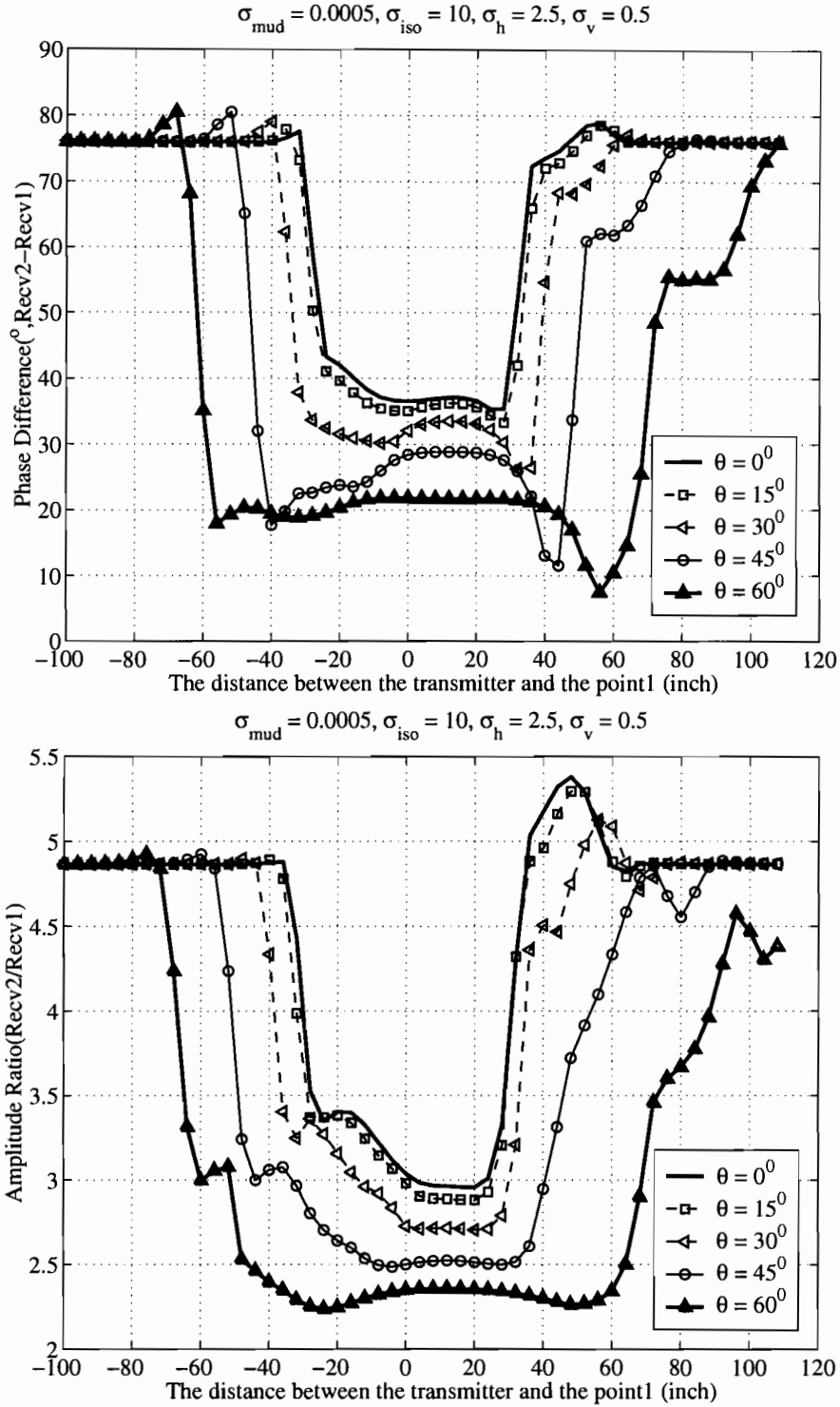


Figure 5.18: Simulation results of the LWD tool using  $\sigma_{mud} = 0.0005[\text{S/m}]$  in an inhomogeneous anisotropic dipping bed with  $\sigma_h = 2.5$ ,  $\sigma_v = 0.5$ , and  $\sigma_{iso} = 10[\text{S/m}]$ (Actual thickness).

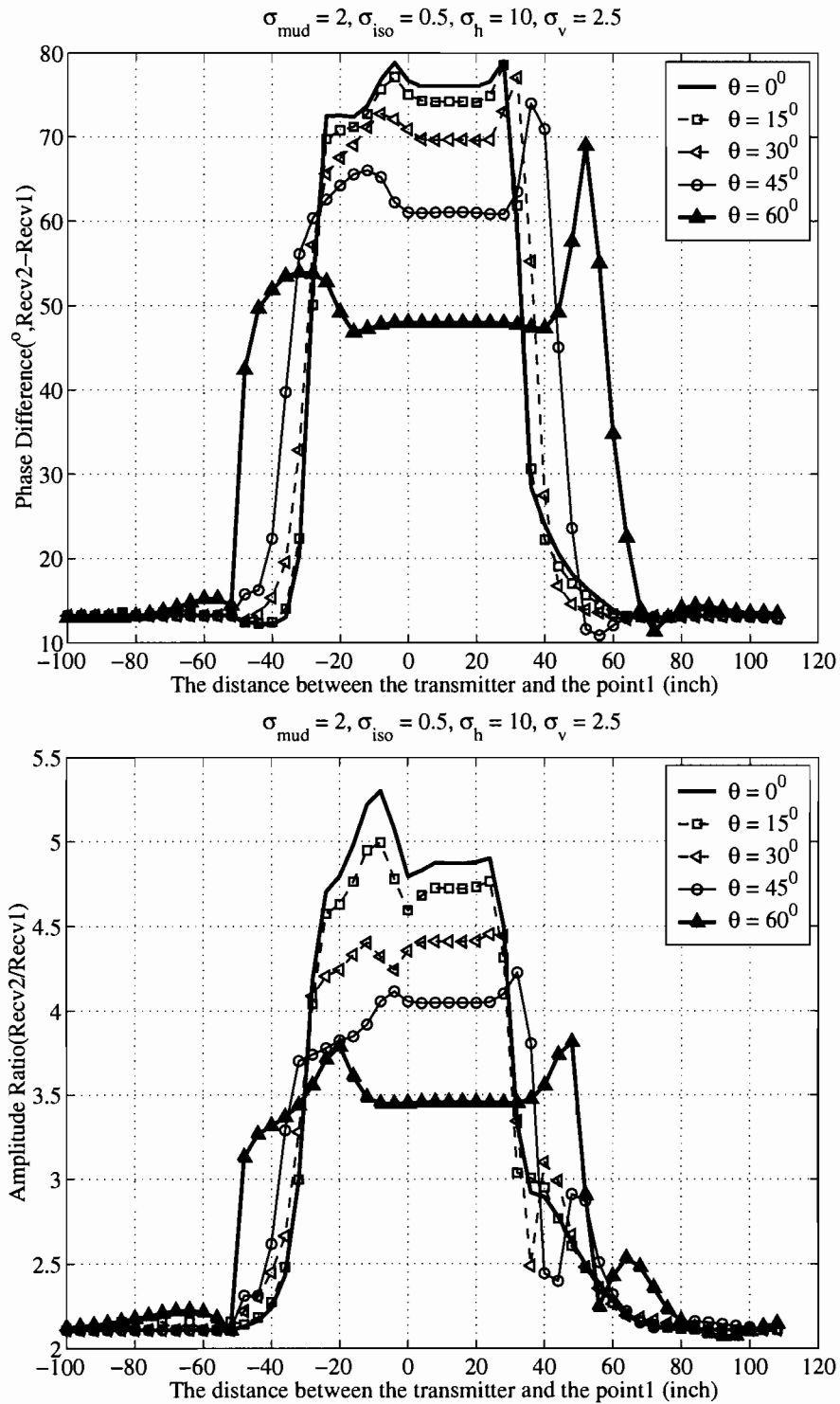


Figure 5.19: Simulation results of the LWD tool using  $\sigma_{mud} = 2[\text{S/m}]$  in an inhomogeneous anisotropic dipping bed with  $\sigma_h = 10$ ,  $\sigma_v = 2.5$ , and  $\sigma_{iso} = 0.5[\text{S/m}]$ (Actual thickness).

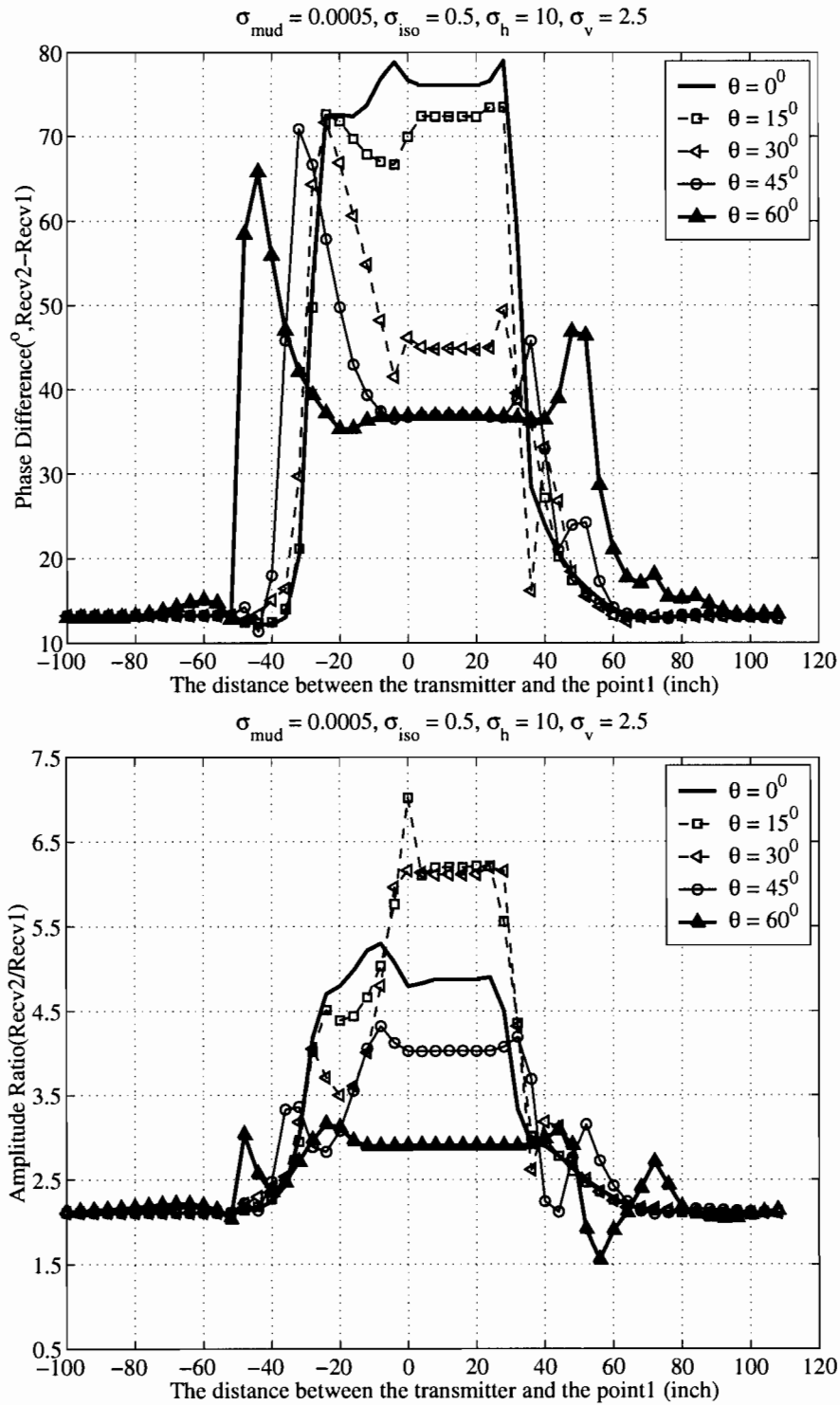


Figure 5.20: Simulation results of the LWD tool using  $\sigma_{mud} = 0.0005[\text{S/m}]$  in an inhomogeneous anisotropic dipping bed with  $\sigma_h = 10$ ,  $\sigma_v = 2.5$ , and  $\sigma_{iso} = 0.5[\text{S/m}]$ (Actual thickness).

## CHAPTER 6

### SUMMARY AND CONCLUSIONS

This thesis has presented the application of the cylindrical FDTD to simulate the responses of electromagnetic logging tools in anisotropic media. In Chapter2, we examined how to represent the generalized conductivity tensor of the earth formation in the tool coordinate system by using the transformation matrix. In Chapter3, we discussed the extension of 3-D FDTD with the anisotropic conductivity tensor to cylindrical coordinates. For computation efficiency, a nonuniform discretization size in  $\rho$  direction is used to enlarge the computation domain. In Chapter4, the two equations-two unknown(2E2U) method was discussed to convert time domain data to frequency domain data. A ramped sinusoidal excitation for the source function was used to avoid DC offset and high frequency contamination. The anisotropic unsplit field formulation of PML is applied to the FDTD algorithm at the outer boundary of the computation domain to avoid spurious reflections from those boundaries. In Chapter5, we presented numerical results of logging tool responses using the extended FDTD method. In Section 5.1-5.3, the LWD tool geometry and discretization were discussed briefly. In Section 5.4.1, the apparent resistivities of the FDTD method in homogeneous anisotropic formations were obtained, showing good agreement with

the results of reference [15] using Sommerfeld integrals. In Section 5.4.2, we studied the effect of the mud conductivity on the tool responses. In section 5.4.3, we study the response of the LWD tool in 3-layer inhomogeneous formations with the anisotropic dipping bed, for various dipping angles. We verified that the responses of the vertical LWD tool,  $\theta = 0^\circ$  in anisotropy formation were controlled by  $\sigma_h$  only. We also verified that the dipping angle affected the apparent thickness of the dipping bed. We simulated the anisotropic dipping bed with the true thickness and actual thickness for various dipping angles. From the examples, the effect of anisotropic dipping bed is clearly observed as the less phase difference and amplitude ratio and the larger horn effect for the higher dipping angle. When the horizontal conductivity on the anisotropic bed was higher than the isotropy conductivity on the background formation and the oil-base mud was used, it was not appreciable to find the dipping bed because of non-monotonic behaviors of the amplitude ratio for the higher dipping angle.

## Future Work

The extended cylindrical FDTD algorithm with full  $3 \times 3$  anisotropy is useful to simulate not only the response of the LWD tool but also other problems involving anisotropic conductivities. However, the unsplit anisotropic PML in cylindrical coordinates used only the real part of the stretching variables in  $\rho$  direction because of instability due to the imaginary part in the present formulation. For this reason, the domain size was larger than that possible with full stretching variables. Our future work will study the stability of an anisotropic PML with full  $3 \times 3$  anisotropy and various well-logging tool scenarios, such as invasion zone, eccentric tools.



## APPENDIX A

### REFERENCE RESULT: LWD TOOL IN INFINITELY THICK BED WITH UNIFORM CONDUCTIVITY

The LWD tool configuration is illustrated in Figure A.1 in homogeneous formation. The LWD tool operates at 2MHz and has a 4-in radius steel mandrel and 5-in radius borehole. The transmitter and receiver antennas consist of 4.5-in radius wire wound around the steel mandrel. The source is chosen to be a ramp sinusoidal excitation. The conductivity of the mud is either  $\sigma_{mud} = 0.0005$  or  $\sigma_{mud} = 2$ [S/m]. The relative permittivity and permeability are equal to be 1. Figure A.2 depicts the responses of the LWD tool in the homogeneous formation with different isotropy conductivities. We note that the phase difference and amplitude ratio of  $\sigma_{mud} = 0.0005$ [S/m] are the same as those of  $\sigma_{mud} = 2$ [S/m]. The domain is discretized by using  $(N_\rho, N_\phi, N_z)=(30, 125, 180)$ . The uniform grid size in  $z$  direction is 2.54 [cm]. In  $\rho$  direction, the discretization size,  $\Delta\rho = 0.635$  [cm] is uniform inside the borehole. Outside the borehole,  $\Delta\rho$  is increased gradually to  $\Delta\rho = 18.7566$  [cm]. The unsplit field PML consists of five cells with a cubic profile for  $a_\rho$  in  $\rho$  direction, and for  $a_z, \rho_z$  in top and bottom regions along the  $z$  direction.

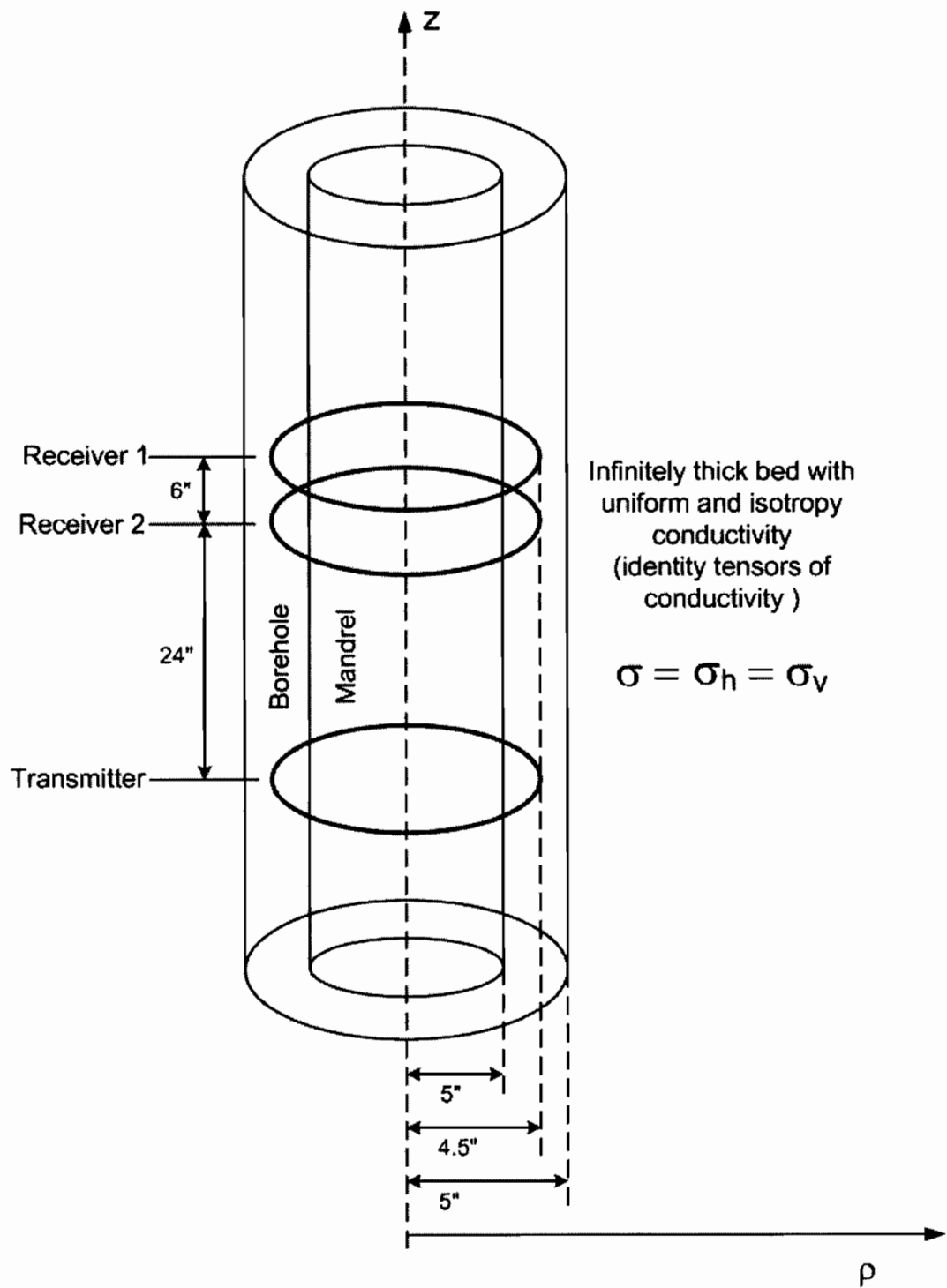


Figure A.1: Illustration of a LWD tool in a homogeneous formation (infinitely thick bed) with an isotropic conductivity

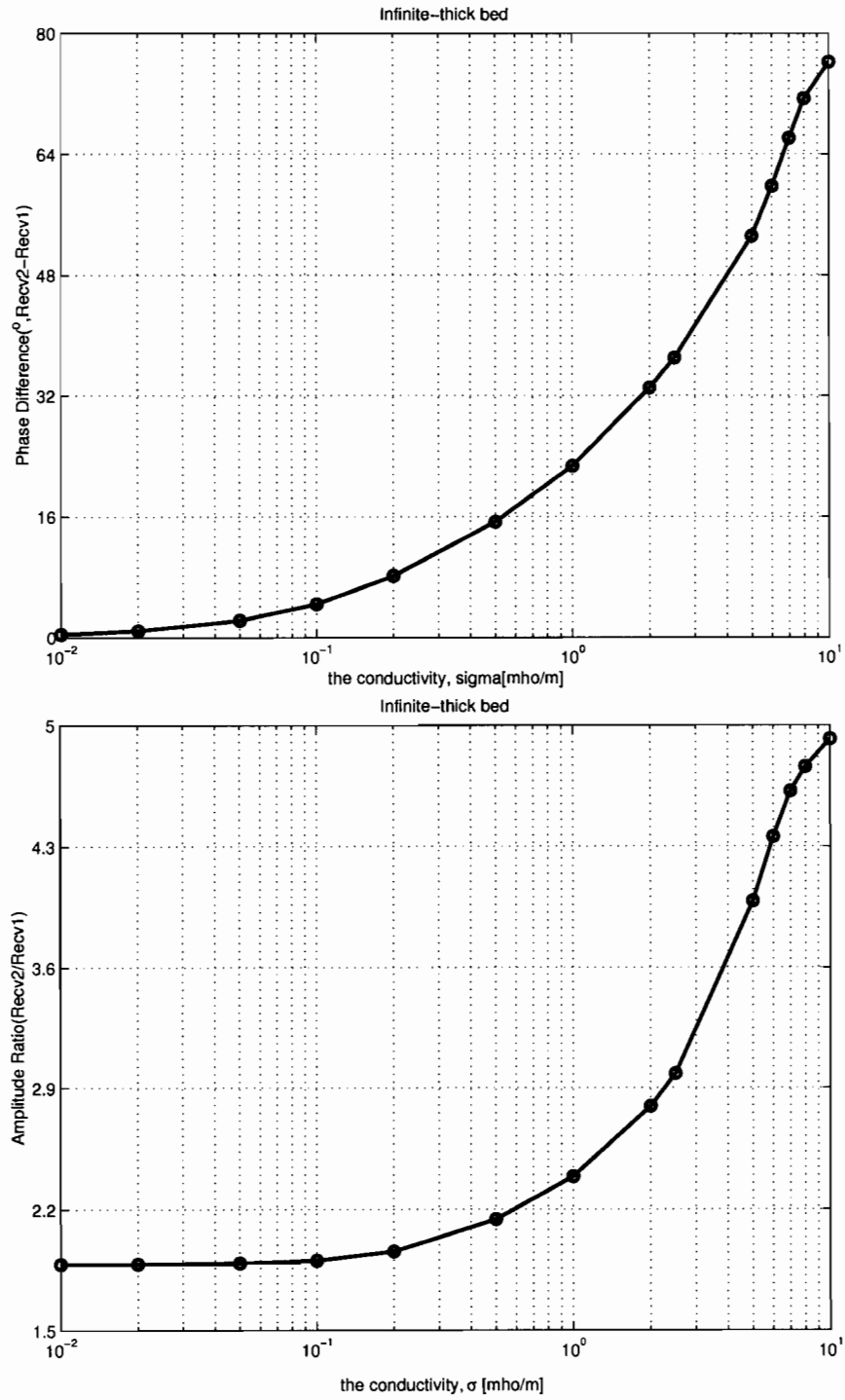


Figure A.2: Simulation of the PD and AR of a LWD tool in an infinitely thick bed with different uniform conductivity,  $\sigma_{mud} = 0.0005$  and  $\sigma_{mud} = 2$  [S/m]

## BIBLIOGRAPHY

- [1] Z. Q. Zhang and Q. H. Liu, "Applications of the BCGS-FFT Method to 3-D Induction Well Logging Problems," *IEEE Trans. Geosci.Remote Sens.*, vol. 41, pp. 998–1004, May 2003.
- [2] G. X. Fan, Q. H. Liu, and S. P. Blanchard, "3-D Numerical Mode-Matching(NMM) Method for Resistivity Well-Logging Tools," *IEEE Trans. Antennas Propag.*, vol. 48, pp. 1544–1522, Oct. 2000.
- [3] Y. Zhang, C. Liu, and L. C. Shen, "The Performance Evaluation of MWD Logging Tools Using Magnetic and Electric Dipoles by Numerical Simulations," *IEEE Trans. Geosci.Remote Sens.*, vol. 43, pp. 1039–1044, July 1996.
- [4] B. Anderson, "Simulation of Induction Logging by the Finite-Element Method," *Geophysics*, vol. 49, no. 11, pp. 1943–1958, 1984.
- [5] T. Wang and S. Fang, "3-D Electromagnetic Anisotropy Modeling Using Finite Differences," *Geophysics*, vol. 66, no. 5, pp. 1386–1398, 2001.
- [6] C. J. Weiss and G. A. Newman, "Electromagnetic Induction in a Fully 3-D Anisotropic earth," *Geophysics*, vol. 67, no. 4, pp. 1104–1114, 2002.
- [7] S. Liu and M. Sato, "Electromagnetic Logging Technique Based on Borehole Radar," *IEEE Trans. Geosci.Remote Sens.*, vol. 40, pp. 2083–2092, Sept. 2002.
- [8] K. S. Yee, "Numerical solution of initial boundary value problems involving Maxwell's equations in isotropic media," *IEEE Trans. Antennas Propag.*, vol. 14, pp. 302–307, 1966.
- [9] J.-Q. He and Q. H. Liu, "A Nonuniform Cylindrical FDTD Algorithm with Improved PML and Quasi-PML Absorbing Boundary Conditions," *IEEE Trans. Geosci.Remote Sens.*, vol. 37, pp. 1066–1072, Mar. 1999.
- [10] A. Taflov and S. Hagness, *Computational Electrodynamics : The Finite Difference Time-Domain Method*. Artech House, Second ed., 2000.

- [11] C. M. Furse, "Faster than Fourier: Ultra-efficient Time to Frequency-Domain Conversions for FDTD Simulations," *IEEE Trans. Antennas Propag. Mag.*, vol. 42, pp. 24–34, Dec. 2000.
- [12] C. M. Furse, D. H. Roper, and D. N. Buechler, "The Problem and Treatment of DC Offsets in FDTD Simulations," *IEEE Trans. Antennas Propag.*, vol. 48, pp. 1198–1201, Aug. 2000.
- [13] F. L. Teixeira and W. C. Chew, "Finite-Difference Computation of Transient Electromagnetic Waves for Cylindrical Geometries in Complex Media," *IEEE Trans. Geosci. Remote Sens.*, vol. 38, pp. 1530–1543, July 2000.
- [14] F. L. Teixeira and W. C. Chew, "On Causality and Dynamic Stability of Perfectly Matched Layers for FDTD Simulations," *IEEE Trans. Microwave Theory Tech.*, vol. 47, pp. 775–785, June 1999.
- [15] J. Allen Q. Howard, "Petrophysics of Magnetic Dipole Fields in an Anisotropic Earth," *IEEE Trans. Antennas Propag.*, vol. 48, pp. 1376–1383, Sept. 2000.
- [16] J. D. Klein, P. R. Martin, and D. F. Allen, "The Petrophysics of Electrically Anisotropic Reservoirs," *Log Anal.*, vol. 38, pp. 25–36, 1997.
- [17] Y.-K. Hue, F. L. Teixeira, L. E. S. Martin, and M. Bitter, "Modeling of EM Logging Tools in Arbitrary 3-D Borehole Geometries Using PML-FDTD," *IEEE Trans. Geosci. Remote Sens.*, vol. 2, pp. 78–81, Jan. 2005.